Understanding and Reducing Warm and Dry Summer Biases in the Central United States: Improving Cumulus Parameterization

Chao Sunda,b and Xin-Zhong Lianga,b

Department of Atmospheric and Oceanic Science, University of Maryland, College Park, College Park, Maryland
 Earth System Science Interdisciplinary Center, University of Maryland, College Park, College Park, Maryland

(Manuscript received 12 April 2022, in final form 24 October 2022)

ABSTRACT: Most climate models still suffer large warm and dry summer biases in the central United States (CUS). As a solution, we improved cumulus parameterization to represent 1) the lifting effect of small-scale rising motions associated with Great Plains low-level jets and midtropospheric perturbations by defining the cloud base at the level of condensation, 2) the constraint of the cumulus entrainment rate depending on the boundary layer depth, and 3) the temperature-dependent cloud-to-rainwater conversion rate. These improvements acted to (i) trigger mesoscale convective systems in unfavorable environmental conditions to enhance total rainfall amount, (ii) lower cloud base and increase cloud depth to increase low-level clouds and reduce surface shortwave radiation, (iii) suppress penetrative cumuli from shallow boundary layers to remedy the overestimation of precipitation frequency, and (iv) increase water detrainment to form sufficient cirrus clouds and balanced outgoing longwave radiation. Much of these effects were nonlocal and nonlinear, where more frequent but weaker convective rainfall led to stronger (and sometimes more frequent) large-scale precipitation remotely. Together, they produced consistently heavier precipitation and colder temperature with a realistic atmospheric energy balance, essentially eliminating the CUS warm and dry biases through robust physical mechanisms.

KEYWORDS: Climate prediction; Cumulus clouds; Bias; Numerical analysis/modeling

1. Introduction

Most climate models have warm and dry summer biases in the central United States (CUS) that persist after decades of physics improvements and resolution increases, diminishing their reliability of climate predictions and scenario projections in the region [see a comprehensive analysis in the companion paper Sun and Liang (2023, hereafter referred to as S&L)]. A recent project for Clouds Above the United States and Errors at the Surface (CAUSES) was established to search for the causes of CUS summer warm biases, and a viable solution (Morcrette et al. 2018; Van Weverberg et al. 2018; Zhang et al. 2018). The project's existing hypotheses categorized the warm biases into three major causes: underestimating precipitation, underestimating low clouds, and misrepresenting land-atmosphere interactions. Since precipitation has a cooling effect (Lin et al. 2017), models that underestimate precipitation may overpredict surface temperature. Most models underestimate clouds in midlatitudes (Cheruy et al. 2014), which leads to overpredicting surface solar radiation and hence temperature. Misrepresenting land processes and interactions with the atmosphere may result in model underestimation of evapotranspiration, which is a leading cause of the warm-and-dry biases (Mueller and Seneviratne 2014; Ma et al. 2018).

© Supplemental information related to this paper is available at the Journals Online website: https://doi.org/10.1175/JCLI-D-22-0254.s1.

Corresponding author: Xin-Zhong Liang, xliang@umd.edu

While these hypotheses are not in full agreement with one another, they are closely linked by how well models simulate convective processes. Unskillful cumulus parameterization may underestimate both precipitation and cloud amounts. Deficit precipitation leads to a drier surface and smaller evapotranspiration, causing model overestimation of Bowen ratio, so more sensible heat flux to the atmosphere (Van Weverberg et al. 2018). Meanwhile, inadequate clouds lead to an overestimation of surface downwelling shortwave radiation. Both effects collaborate to induce summer warm-and-dry biases in CUS. Furthermore, models rely on a skillful cumulus scheme to realistically simulate the land–atmosphere coupling strength (Guo et al. 2006). Taken together, the model representation of the convective process is the central argument connecting the three hypotheses on the warm-and-dry biases.

Current cumulus parameterization schemes still suffer many difficulties in capturing convection characteristics in CUS (Liang et al. 2004a; Klein et al. 2006; Qiao and Liang 2015, 2016, 2017; Gao et al. 2017; Sun and Liang 2020a,b). Two unique summer climate features of CUS may challenge skillful cumulus parameterization. First, considerable convection activities can occur in CUS under weak large-scale forcing conditions and even unfavorable environments (Song et al. 2019). Early observational studies recognized those weakly forced yet highly impactful convections (e.g., the northwest-flow severe weather outbreaks) as the preexisting synoptic circulation for MCSs to occur (Johns 1993; Stensrud and Fritsch 1994). More recent observations showed that small-scale upward motions could form in the left exit region of the Great Plains low-level jets (LLJ) or ahead of subsynopticscale midtropospheric perturbations to overcome existing convective inhibitions (CIN) and hence trigger mesoscale convective systems (MCS) in unfavorable environments (Augustine and Caracena 1994; Moore et al. 2003; Wang et al. 2009, 2011; Wang and Clark 2010; Marsham et al. 2011; Geerts et al. 2017; Pokharel et al. 2019; Chasteen et al. 2019; Parish et al. 2020). These MCSs may be associated with more than half of total precipitation in CUS (Wang et al. 2009; Feng et al. 2019, 2021; Hu et al. 2020, 2021). Thus, neglecting the lifting effect of these subgrid updrafts can cause a cumulus parameterization scheme to significantly underpredict convective precipitation in CUS.

Second, cirrus clouds are the most frequent cloud type observed in summer CUS (Kollias et al. 2007). They significantly reduce outgoing longwave radiation (Hartmann et al. 2001) and modulate precipitation through diabatic cooling changes (Muller and O'Gorman 2011). They can form a persistent upper cloud ice shield to increase the static stability, which is a crucial negative feedback suppressing convective activity (Fowler and Randall 1994). Climate models may underestimate these high-level clouds in summer over CUS (e.g., Joos et al. 2008; Kay et al. 2012; Evans et al. 2017), although their bias evaluation was still very limited, lacking regional specification or by large observational uncertainty (Zhang et al. 2005; Tselioudis et al. 2021). The underestimation of high thin clouds may imply that the modeled cirrus lifetime is too short, preventing them from being advected to have a downstream effect, or cirrus clouds may also be quickly burned off by strong absorption of upwelling longwave radiation from below unless they lie above lower cloudy layers (Hartmann et al. 2001). Thus, anvils that coexist with deep convective towers can be expected to be more effective for changes in diabatic cooling. In both cases, underestimated cirrus clouds and their consequences on surface climate may indicate cumulus parameterization deficiencies.

This study aims to understand and reduce the warm-and-dry summer biases in CUS through improving the cumulus parameterization (for deep convection) by incorporating the two overlooked climate features discussed above. Section 2 articulates the improvements to the cumulus scheme in the regional Climate–Weather Research and Forecasting Model (CWRF; Liang et al. 2012). Section 3 describes the model experiments, observational data, and analysis methods. Section 4 compares the results of CWRF using the cumulus scheme with and without the improvements. Section 5 explores the physics mechanisms for the improved cumulus parameterization to reduce the warm-and-dry biases. Section 6 gives the summary and conclusions.

2. Cumulus parameterization improvements

This study used CWRF (Liang et al. 2012) as the test bed for improving cumulus parameterization to reduce the dry-and-warm biases in CUS (see Table 1 for the list of key acronyms). The CWRF has incorporated an ensemble cumulus parameterization (ECP) based on Grell and Dvénéyi (2002) with major improvements detailed in Qiao and Liang (2015, 2016, 2017). The ECP has demonstrated reliable performance over ocean (Qiao and Liang 2016), land (Qiao and Liang 2017), other climate regimes (Liang et al. 2019; Li et al. 2021;

TABLE 1. Summary of key acronyms used in this study.

Term	Meaning
$\overline{C_0}$	Autoconversion parameter
C0T	Experiment using the temperature-dependent
	autoconversion parameterization scheme
CAUSES	Clouds Above the United States and Errors at the
	Surface
CIN	Convective inhibition
CTL	Control experiment
CUS	Central United States
CWRF	Regional Climate-Weather Research and
	Forecasting Model
ECP	Ensemble cumulus parameterization
JST	Experiment using the JS trigger plus the Tokioka
	constraint
JS trigger	Jakob and Siebesma (2003) trigger
LCL	Lifting condensation level
LFC	Level of free convection
LLJ	Great Plains low-level jets
LW_d	Longwave downwelling flux at surface
LW_{tot}	Total longwave cooling (LW _{tot} = LW _d - LW _u + OLR)
LW_{u}	Longwave upwelling flux at surface
MCS	Mesoscale convective systems
NCP	New cumulus parameterization
OLR	Outgoing longwave radiation
PR	Daily mean precipitation amount
SH	Sensible heat flux at surface
SW_d	Shortwave downwelling flux at surface
SW_{tot}	Total shortwave cooling
	$(SW_{tot} = SW_d - SW_u + SW_u^{toa})$
SW_u	Shortwave upwelling flux at surface
SW_u^{toa}	Shortwave upwelling flux at top of the atmosphere
T_2	2-m temperature

Jiang et al. 2021), and for extreme precipitation (Qiao and Liang 2015; Sun and Liang 2020a). The ECP has built-in parameterization for both deep and shallow convections. This study used ECP only for deep convection and the parameterization developed by Park and Bretherton (2009) for shallow convection.

This study improved the ECP scheme [hereafter referred to as the new cumulus parameterization (NCP)] by incorporating three major changes: 1) the convection trigger function, 2) the entrainment rate constraint, and 3) the cloud water conversion rate. While the specific formulations for these changes are presented in the online supplemental material, their rationale and principles are outlined below.

As discussed earlier, LLJs and midtropospheric perturbations can induce subgrid updrafts that overcome the negative buoyancy barrier of CIN and thus lift parcels to the level of free convection (LFC), triggering MCS in unfavorable environments. Some attempts to parameterize the effect of unresolved updrafts were to define the cloud base at the level of condensation (LCL) (Donner 1993; Hong and Pan 1998). In particular, Jakob and Siebesma (2003) developed a new parcel ascent model-based trigger function that explicitly predicts the updraft vertical velocity and defines the cloud base at the

TABLE 2. Observations, resolutions, available years, and their references.

Meteorology variable	Temporal (years) spatial resolution (mapping method)	Source	
Precipitation (hourly)	Hourly (2002–19) 4-km grid (conservative)	NCEP stage IV gauge-adjusted radar- based data (Lin and Mitchell 2005)	
Precipitation (daily)	Daily (1979-2019) 4-km grid	gridMET: Daily surface weather data	
2-m temperature	(conservative)	(Abatzoglou 2013)	
Short- and longwave radiation at surface and top of atmosphere (clear/all)	Monthly (1984–2007) $1^{\circ} \times 1^{\circ}$ lat–lon grid (linear)	The NASA/GEWEX Surface Radiation Budget (SRB) (Gupta et al. 1999)	
Cloud fraction, cloud-top pressure, cloud optical depth	Monthly (2002–19) $1^{\circ} \times 1^{\circ}$ equal-angle grid (linear)	MODIS cloud optical properties: The Collection 6/6.1 level 2 (Platnick et al. 2015)	
Height, zonal and meridional winds, omega, temperature, humidity	Monthly (1979–2019) 32-km grid with 29 pressure levels (linear)	NCEP North American Regional Reanalysis (NARR) (Mesinger et al. 2006)	

LCL. (Note that these subgrid parcels or updrafts are represented as a collective ensemble and parameterized in terms of resolved quantities.) This function, hereafter referred to as the JS trigger, was tested with the Tiedtke (1983) cumulus parameterization that led to an overall improved ECMWF forecast performance (Bechtold et al. 2008).

This study incorporated into ECP the JS trigger, which decides whether a convection occurs and where its cloud base and top are located (following the implementation by Zhang and Wang 2017). The original ECP defines the cloud base at LFC, which is estimated as follows. It first searches upward for the layer with the maximum moist static energy. If this layer is higher than 4000 m above the surface, no convection occurs. Otherwise, it sets the cloud base to this layer for a deep convection. The cloud top is located at the layer of zero buoyancy.

The JS trigger uses an entraining plume model to predict the updraft vertical velocity w_u in the convective boundary layer depending on buoyancy and near-surface perturbations. It defines the cloud base at the discrete model level closest to LCL at which $w_u > 0$ and the cloud top at which w_u vanishes. The first parcel departure level is set at the second layer for deep convections. At this level, turbulent perturbations parameterized in terms of surface sensible and latent heat fluxes are added to the parcel's temperature and humidity, respectively. A deep convection occurs if the cloud depth is thicker than 200 hPa. Otherwise, it tests sequentially the parcels departing from higher levels (below ~ 500 hPa) with constant perturbations $(0.2 \text{ K}, 10^{-4} \text{ kg kg}^{-1})$ until finding deep convection.

The JS trigger thus assumes that the updraft induced by turbulent perturbations serves as the pseudobuoyancy to overcome existing CIN, lifting the parcel to penetrate through LCL and further LFC. In addition, we adopted the constraint of Tokioka et al. (1988) to prevent deep penetrative convection if the PBL is too shallow, that is, set $w_u = 0$ so no convection occurs if the entrainment rate of environmental air is smaller than a threshold inverse of the PBL height. While the PBL height is provided by the CAM PBL scheme (improved Holtslag and Boville 1993), the entrainment rate is parameterized following Bechtold et al. (2008).

Anvil cirrus clouds typically accompany deep convections. An essential but often underappreciated parameter in cumulus parameterization is the cloud-to-rainwater conversion rate C_0 (Emanuel and Živković-Rothman 1999), which generally increases with air temperature for the ice phase microphysical process (Fletcher 1962). Neglecting this dependency tends to underestimate water detrainment to form sufficient cirrus clouds (Lim et al. 2014; Han et al. 2017; Goswami et al. 2020). We adopted the C_0 increase with temperature from Han et al. (2016), except replacing the exponential dependence with a sigmoid function for a more gradual slope (see appendix A).

3. Model experiments, observational data, and analysis methods

This study conducted two 40-yr continuous CWRF integrations from 1 October 1979 to 1 January 2020 at 30-km grid spacing over the well-tested North American domain, including the contiguous United States (Liang et al. 2012). The control simulation (CTL) used the CWRF default physics configuration [see Sun and Liang (2020a) for details], including ECP for cumulus parameterization. The second simulation (NCP) used the identical configuration except incorporating into ECP all the improvements presented in section 2. To understand the physical mechanisms causing the improved model results, four additional branch runs were made, each of which was a warm start from the CTL simulation conditions on 1 May for a 4-month integration that ended on 1 September each year between 1980 and 2020. One run adopted both the JS trigger and the Tokioka constraint to determine the combined convection activation (JST), while the others included separately one of the two activations and the temperature-dependent autoconversion parameter C_0 (C0T). The warm start helped remedy the complication by soil memory effects to focus on the ECP changes. All CWRF simulations were driven by lateral boundary conditions derived from the latest European Centre for Medium-Range Weather Forecasts reanalysis (version 5, hereafter ERA5), with 6-hourly data available at a grid spacing of 0.25° (Hersbach et al. 2020). The analyses below were based on summer (1 June-31 August) during 1980-2019.

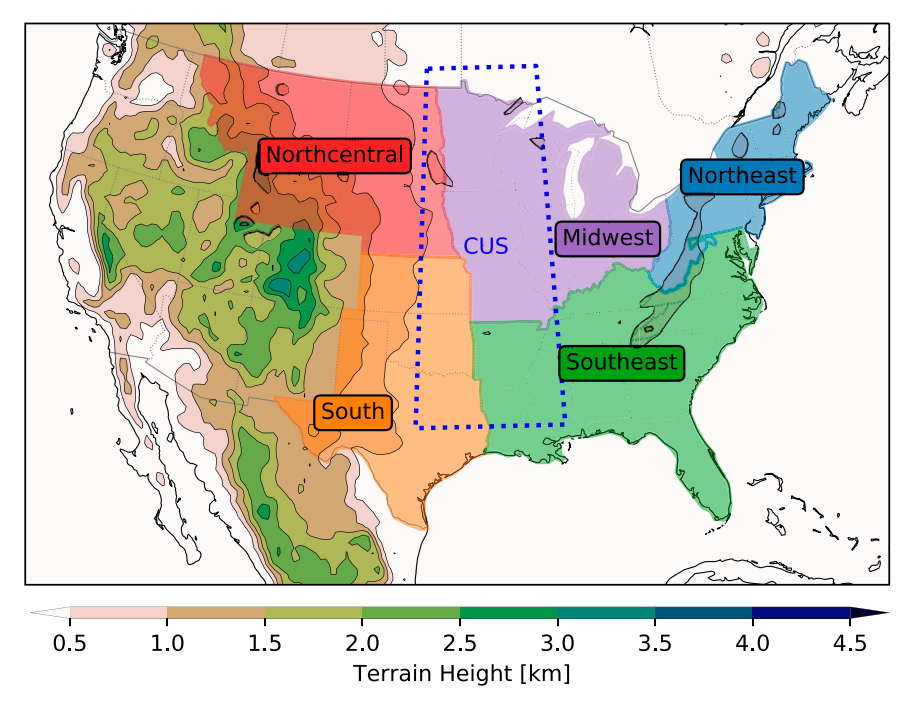


FIG. 1. Characteristic climate regions (colored boundaries with names) along with the CUS key area (blue dotted outline enclosing 31° – 52° N, 89° – 98° W) where the warm-and-dry bias is most significant as defined in the CAUSES project. The color contour map shows the terrain height distribution.

Table 2 summarizes the observational data used in this study, including their source, period, resolution, and mapping method onto the CWRF 30-km grid. In particular, daily precipitation and surface air temperature data were from the high-resolution (4-km) gridded surface meteorological analysis of Abatzoglou (2013), available from 1979 onward. Other data include surface downwelling shortwave and longwave radiation fluxes, cloud amounts in categorical bins of pressure and optical depth, and atmospheric circulation variables (geopotential height, wind, air temperature, and specific humidity).

The major characteristic regions affected by changing ECP to NCP include CUS defined in the CAUSES project and the Midwest, North-Central, South, and Southeast typically used as the key U.S. climate regions. These are illustrated in Fig. 1 along with the terrain distribution and used below to elaborate the result comparison and process understanding.

To facilitate the physical understanding of the results by various changes to ECP, two decomposition analyses were performed. First, following Zhang et al. (2018) and Van Weverberg et al. (2018), the net surface shortwave or longwave radiation biases were decomposed into contributions from the surface (shortwave reflection or longwave emission), total cloud, and integrated water vapor. Comparison of these component differences helped identify whether the ECP changes reduced model biases in a physically consistent manner and which key processes induced these bias reductions. Second, following Muller and O'Gorman (2011), the precipitation-related latent heat release was separated into the column-integrated dry static energy divergence and total diabatic cooling that consists of the

atmospheric net radiative loss minus the gain from surface sensible heat flux. This separation helped quantify the radiative contribution to the precipitation change associated with the ECP improvements.

The CWRF has a unique Conjunctive Surface-Subsurface Process model (CSSP) to realistically capture the detailed terrestrial hydrology and land-atmosphere interaction (Dai et al. 2003, 2004; Liang et al. 2005a; Choi et al. 2007, 2013; Choi and Liang 2010; Yuan and Liang 2011; Liang et al. 2012; Xu et al. 2014; Gan et al. 2015; Ji et al. 2017). This facilitates the present study to focus on cumulus parameterization improvements, assuming that the CSSP coupling well represents the interactions between surface and convection processes. In addition, CWRF has implemented the latest satellite Cloud Feedback Model Intercomparison Project Observation Simulator Package version 2 (COSP; Bodas-Salcedo et al. 2011; Swales et al. 2018) to simulate cloud characteristics that are consistent with satellite retrievals. The COSP allows a direct comparison with satellite observations, which is needed to evaluate how our proposed ECP changes affect coupling convection, cloud, and radiation processes.

4. Reduction of CUS warm-and-dry biases

Figure 2 compares the 1980–2019 averaged summer biases in surface air temperature, precipitation, surface downwelling shortwave radiation, and top-of-the-atmosphere outgoing long-wave radiation (OLR) between the CWRF using the control (CTL) and new (NCP) cumulus parameterization. Similar to the Coupled Model Intercomparison Project (CMIP) result,

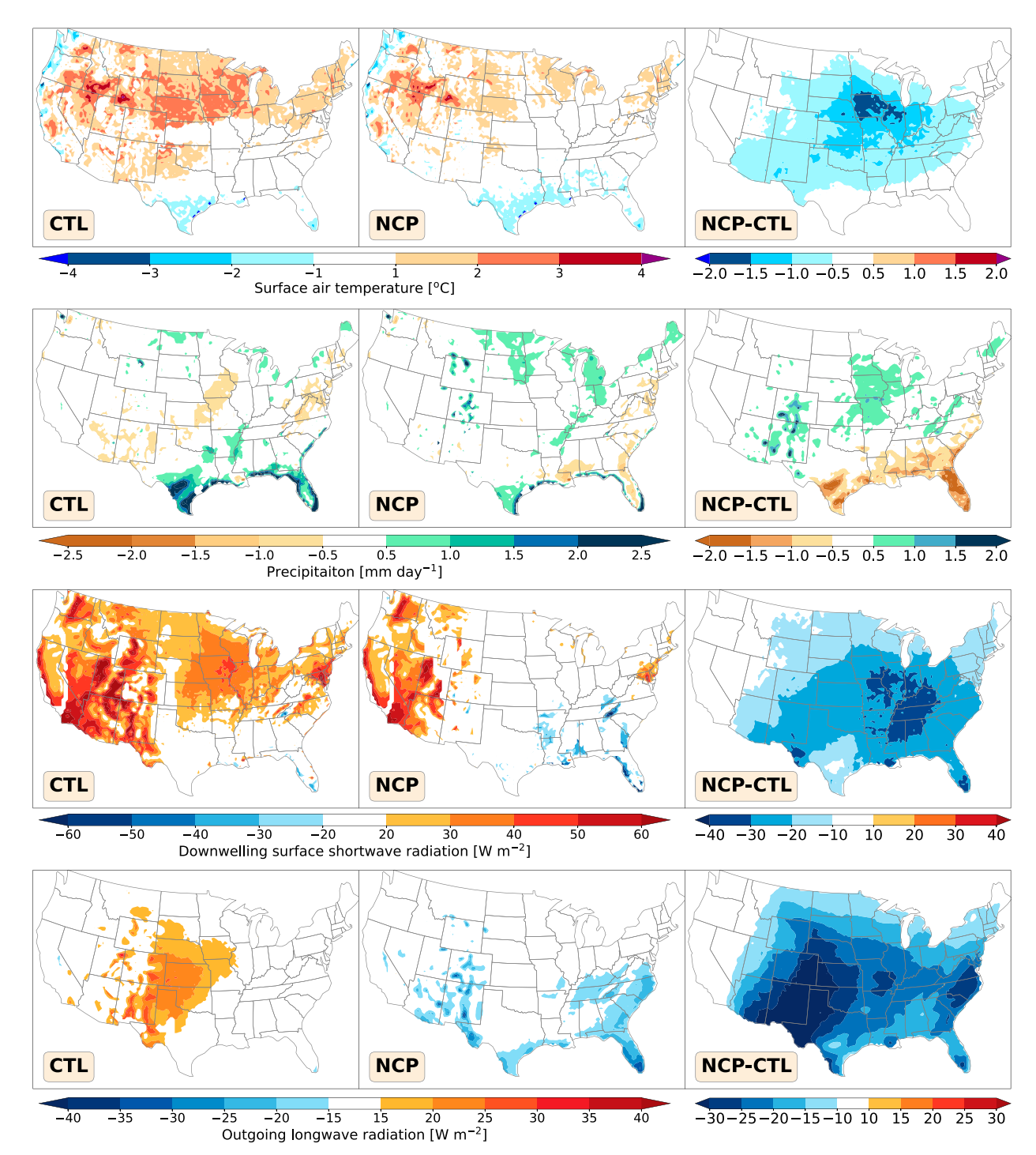


FIG. 2. Summer biases in surface air temperature ($^{\circ}$ C), precipitation (mm day $^{-1}$), and surface downwelling shortwave and top outgoing longwave radiation fluxes (W m $^{-2}$) simulated by CWRF using the control (CTL) and new (NCP) cumulus parameterization. The temperature and precipitation biases are averaged over the whole integration period (1980–2019), while the radiation bias over a shorter period (1984–2007) as limited by available observations.

CTL simulated significant warm biases in CUS, most prominent ($>2^{\circ}$ C) in the Midwest and North-Central (see Fig. 1 for the specification of the key climatic regions). It also had warm biases of \sim 2°C over the Rocky Mountain regions, resembling

high-resolution CMIP results (Fig. 1 in S&L). In contrast, NCP largely eliminated the warm biases around CUS, with most areas reduced to <1°C. The reduction is evident on the NCP - CTL map concentrated in the Midwest.

For precipitation, CTL simulated significant dry biases $(\leq -1 \text{ mm day}^{-1})$ in CUS and some areas of the southern Rocky and the Appalachian Mountains. Meanwhile, it had wet biases over the Gulf states, most pronounced in south Texas. NCP mostly eliminated the dry biases over CUS and the southern Rocky Mountains region. It also largely suppressed the overestimation in the Gulf states, albeit overdone so in some areas away from the coast. This suppression is clearly seen on the NCP - CTL map to occur over broad regions across the Southeast, mainly due to the constraint of Tokioka et al. (1988). As shown in Fig. S1 in the online supplemental material, this constraint significantly reduced the number of rainy days over the Great Plains and Southeast, led to locally less precipitation and drier soil moisture with deficit water available for surface evaporation, and so caused a drier and deeper PBL under similar surface sensible heating, that is, elevated PBL height (Troen and Mahrt 1986). Remotely, more abundant water vapor was transported downstream to yield more precipitation in the Midwest and northern Southeast. On the other hand, NCP slightly enhanced the wet biases in the northern states, which may be related to rainfall overestimation by cloud microphysics processes. It also produced more excessive precipitation on many spots in Wyoming and Colorado, mostly along the windward slope of local terrain peaks east of the Rocky Mountains. This amplification was mainly due to the JS trigger (Fig. S2). It may suggest that some constraint is needed to prevent the JS trigger from activating convection too easily because of local orographic lifting. The role of lower tropospheric perturbations that induce small-scale updrafts to trigger MCS may be overestimated as they are relatively rare on the windward of the Rocky Mountains (Wang et al. 2009).

For surface shortwave radiation, CTL produced substantial overestimates in the Midwest and Northeast (20–60 W m⁻²), with a spatial pattern highly correlated with that of temperature biases. It had smaller overestimates in the North-Central, which did not correspond well to the center of warm biases. Weak correspondences were also simulated in the western states, especially in the Southwest, where excessive radiation happened with warm or small temperature biases. NCP essentially eliminated the radiation biases in most areas across the North-Central, Midwest to Northeast, generally below 10 W m⁻² or within observational uncertainty. As clearly shown on the NCP - CTL map, the systematic insolation reduction (by 20-40 W m⁻²) extended to also cover the entire South to Southeast. This reduction was somewhat overdone to cause underestimates (by 10-20 W m⁻²) in some areas of the Southeast, coincident with slightly colder biases along the Gulf coast. It was a combined result of the Tokioka constraint and COT effect (Fig. S2), increasing total cloud amount (Fig. S3).

For OLR, CTL simulated substantial overestimates across the southern to central Great Plains and the western part of the Midwest (15–30 W m⁻²), indicating that high-level clouds were significantly underestimated. NCP eliminated the biases in most areas across the region. As shown on the NCP – CTL map, the systematic OLR reduction (by 10–30 W m⁻²) extended to also cover the entire eastern United States. As designed, C0T significantly increased high–middle clouds (Fig. S3),

which overcame the large underestimate in CTL and further reduction by the Tokioka constraint eliminating convection occurrences from shallow PBL (Fig. S1). The OLR reduction was overdone to cause underestimates (by 15–20 W m⁻²) in the South to Southeast coastal regions, coincident with drier biases

Figure 3 compares summer composite biases of total precipitable water and vertically integrated moisture transport flux when daily precipitation averaged over a key region (i.e., the Midwest, North-Central, South, and Southeast) exceeds its climatological median. Observations showed a southerly LLJ prevailing over the Great Plains along the western flank of the Bermuda high. The LLJ and its associated moisture transport were much stronger in the composites for the above-median precipitation events in the Midwest and North-Central than those in the South and Southeast. This is consistent with the observed interannual teleconnection pattern in which westward extension of the Bermuda high enhances the Great Plains LLJ that transports more moisture northward to cause precipitation increases in the Midwest and decreases in the Gulf states (Zhu and Liang 2013). For all composites, CTL produced systematically less precipitable water (i.e., drier atmosphere) over the Gulf of Mexico, Southeast, and CUS, while transporting more moisture toward New England through the channel over the western North Atlantic. NCP largely eliminated all these regional circulation biases.

Figure S4 compares the latitude–pressure cross-section composites of specific humidity, and meridional–vertical wind biases averaged across the longitudinal span of CUS for the same above-median precipitation events in the four regions. CTL simulated stronger upward motions over the Gulf of Mexico and coastal states, driving locally more convective precipitation while causing remotely larger subsidence over the central Great Plains. Both effects depleted more moisture from the column between 800 and 500 hPa, resulted in a drier lower troposphere across 22°–40°N. Again, NCP largely corrected these regional circulation biases.

Given their critical role in linking CUS warm and dry biases as revealed from the CWRF NCP sensitivity (Fig. 2), the net (downwelling minus upwelling) surface shortwave and longwave radiation flux biases were decomposed into the contributions from the column (vertically integrated) cloud and water vapor as well as surface reflection or emission, following the method of Zhang et al. (2018) and Van Weverberg et al. (2018). Figure 4 compares these bias compositions between CTL and NCP, while Fig. S5 shows the NCP minus CTL differences in the net fluxes and their relative changes to the observed means. The net shortwave biases were mostly positive in CTL and about twice the magnitude of the net longwave biases, which were positive in CUS and eastern coast states but negative in the western states. NCP significantly reduced the biases for both shortwave and longwave fluxes over most areas from the central to eastern states. [Note that the bias reduction relative to the observed mean is larger in the longwave than shortwave flux (Fig. S5).] Small changes were simulated in the western states, where the Rocky Mountains play a dominant role in the prevailing weather patterns.

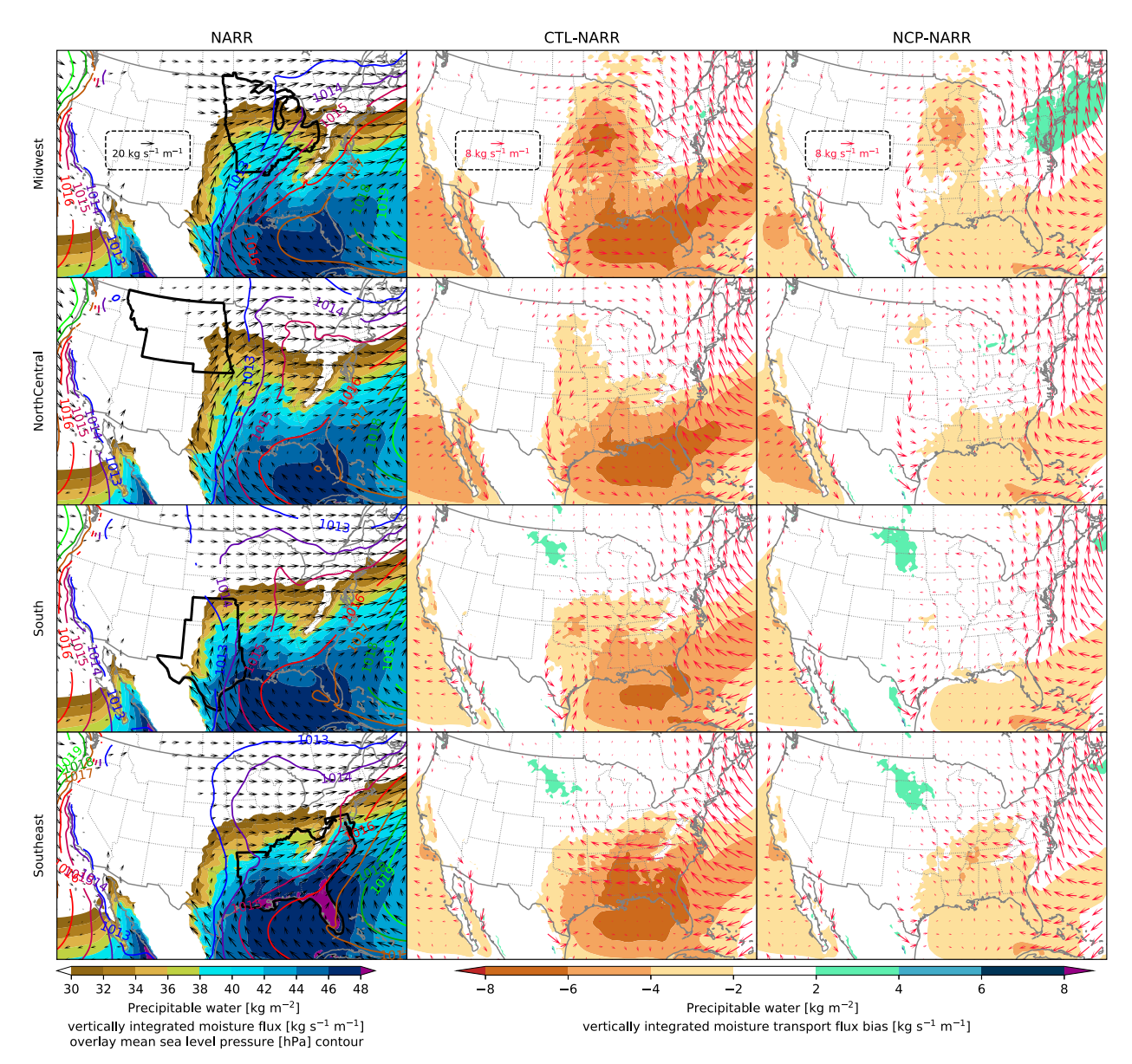


FIG. 3. Summer composites of total precipitable water (kg m⁻²; color fill), mean sea level pressure (hPa; color contour lines) and vertically integrated moisture flux (kg m⁻¹ s⁻¹; vectors) when daily precipitation averaged over a key region (enclosed in a thick black outline) exceeds its climatological (1980–2019) median. (left) The NARR reference overlaid with sea level pressure (hPa; color contours), and (center),(right) CWRF CTL and NCP biases from NARR. (top to bottom) Our key composite regions: the Midwest, North-Central, South, and Southeast.

For shortwave, cloud biases dominated most regions while water vapor biases play a second important role in eastern United States. Insufficient low clouds (see below) reflected less while inadequate water vapor amounts (Fig. 3) absorbed less, both of which led to more insolation to the surface. The contribution from surface reflection biases was relatively small, likely because CWRF incorporates a realistic albedo parameterization (Liang et al. 2005b), which was not changed between NCP and CTL. Minor reflection changes might occur as wetter soil from more precipitation has lower albedo. For longwave, cloud biases dominated the Rocky Mountains

while water vapor biases played a more important role in CUS. Insufficient clouds emitted less, causing negative downwelling radiation biases over the Rockies. In contrast, inadequate water vapor amounts were identified with positive radiation biases in CUS and also, albeit weaker, in the Midwest and Northeast. This occurred because the water vapor effect on longwave radiation is considerably stronger when it is wet than dry—the less frequent wetter conditions may cause excessive radiation in total even in a drier atmosphere on average (Van Weverberg et al. 2018). Note that surface emission biases mainly reflected ground temperature biases,

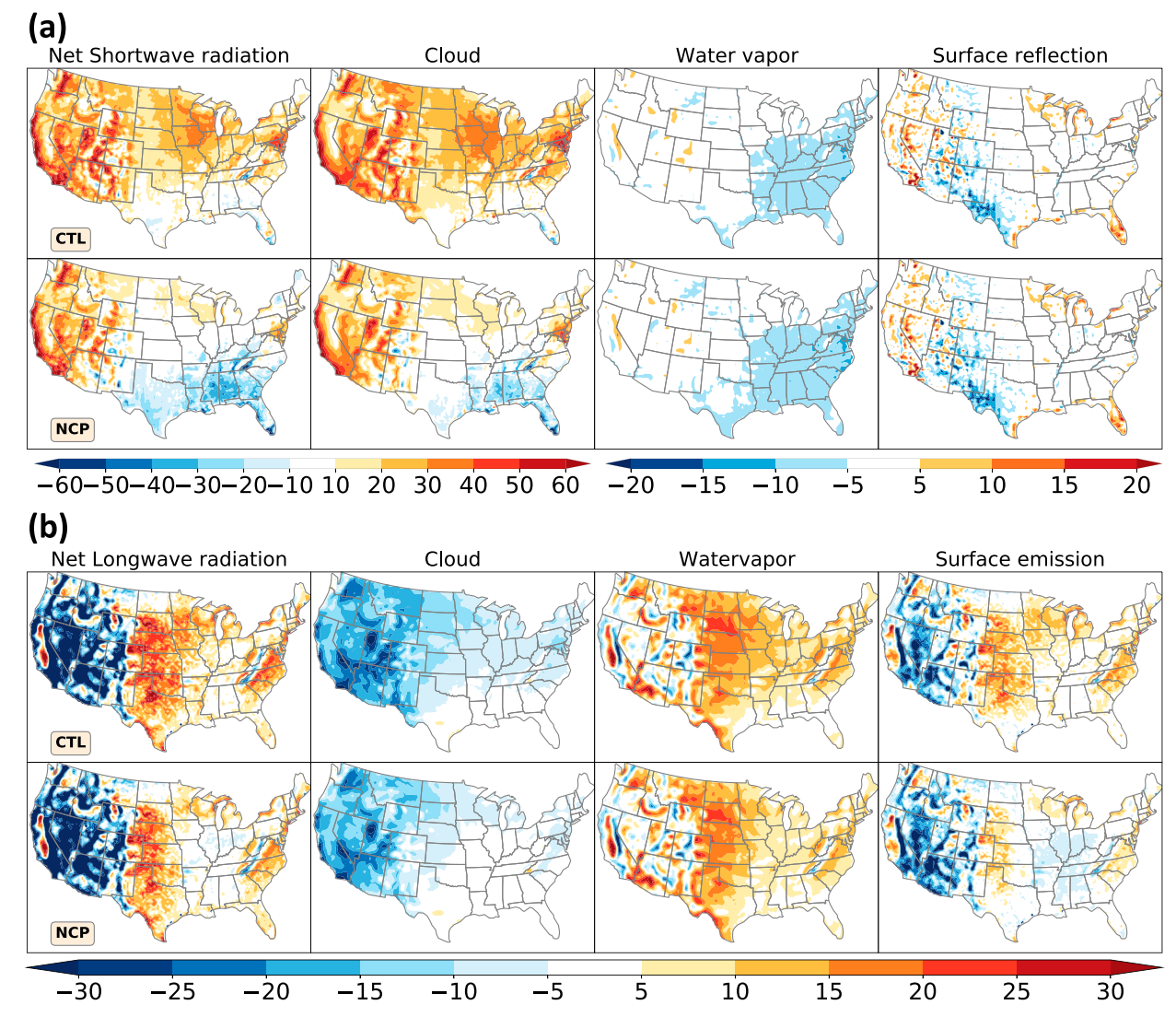


FIG. 4. CWRF summer surface net (a) shortwave and (b) longwave radiation (W m⁻²) biases from SRB observations during 1984–2007, comparing CTL and NCP. (left to right) Total biases and their contributions to induced column cloud and water vapor as well as surface reflection or emission biases.

which were closely related to surface air temperature biases (S&L).

For both shortwave and longwave radiation biases, the most remarkable improvement by NCP over CTL was the significant reduction of cloud underestimates. The NCP – CTL maps reveal close correspondences of increased low and midhigh clouds (Fig. S3) with, respectively, decreased surface downwelling shortwave and top outgoing longwave fluxes (Fig. 2). Given their importance, cloud biases were further separated by their top pressures and optical depths. Figure 5 compares these statistics averaged over the four key regions. CTL underestimated optically thin and thick clouds in both low and high layers over all regions except for overestimated thick low clouds in the Southeast. CTL also underestimated thin but overestimated thick middle clouds over all regions. Thus, in CTL, insufficient low and high cloud amounts

contributed most to the cloud-induced radiation biases. In the Midwest, North-Central, and Southeast, NCP systematically improved both thin and thick low and middle clouds as well as thick high clouds. Exceptions occurred in the South, where NCP underestimated thin middle clouds but overestimated thick low clouds. Therefore, NCP simulated overall more realistic cloud amounts in both vertical distribution and optical depth to largely reduce surface radiation budget biases and essentially eliminate CUS warm-and-dry biases.

An important question is how NCP changed (from CTL) the frequency and intensity between convective (parameterized) and large-scale (resolved) precipitation events. As shown in Fig. S3, NCP significantly increased convective rainy days over two major clusters. One cluster extended across the Great Plains and the neighboring western states, where more frequent deep convections (starting from high elevations)

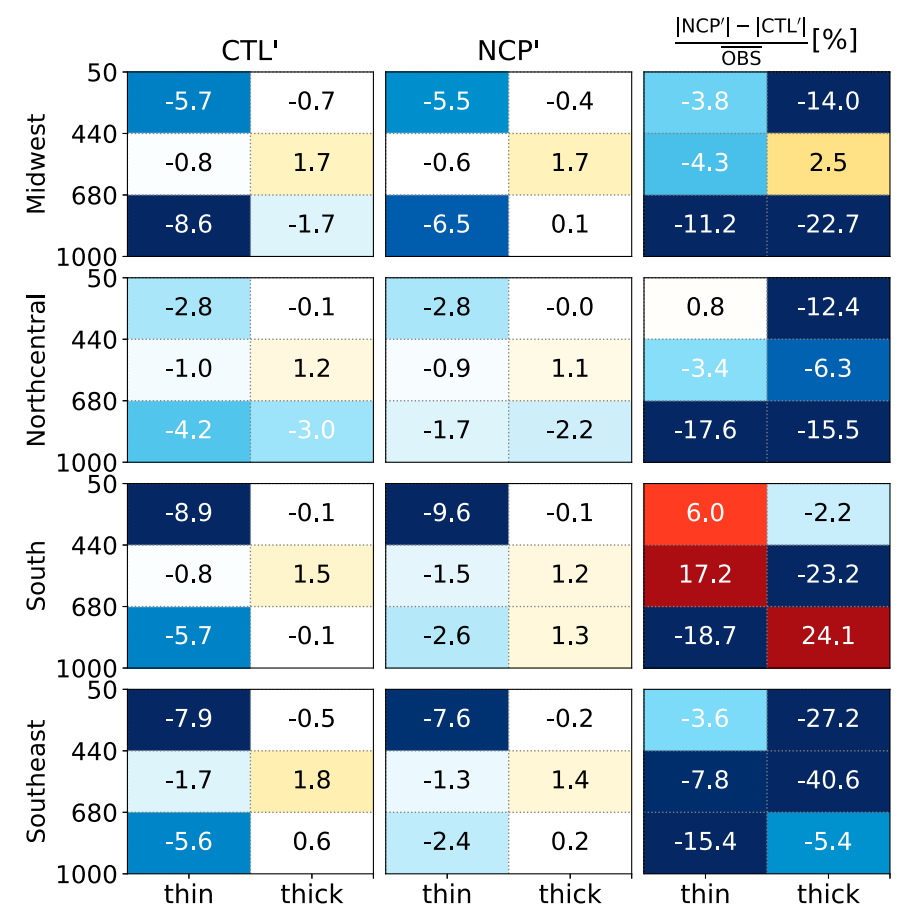


FIG. 5. CWRF summer cloud amount biases from MODIS averaged 2002–19 in each bin of joint pressure (vertical) and optical depth (horizontal) over the four key regions, comparing biases (denoted by a prime) of (left) CTL and (center) NCP as well as (right) relative differences of their absolute biases (%; |NCP'| minus |CTL'| over the observed mean of MODIS). The actual bias value ($\times 100$) is listed with a warmer (cooler) color for a larger overestimation (underestimation). A cooler (warmer) color for the relative difference indicates improvement (deterioration).

produced more cirrus clouds to mostly eliminate the OLR overestimates in CTL, with little effect on surface shortwave radiation. Another cluster extended across the Midwest and Southeast, where more deep convections (starting from low elevations) produced more low–midlevel clouds to significantly reduce both surface insolation and OLR overestimates in CTL. Meanwhile, more frequent triggering of convections removed instability energy and water vapor (by rainout) more quickly so to reduce convective rainfall intensity, especially in the downstream regions (such as eastern Great Plains). On the other hand, weaker convective precipitation allowed the air to be more saturated and hence increased large-scale rainy days, especially in the downstream regions of the two clusters. For the same reason, large-scale rainfall intensity was generally enhanced over most regions.

5. Physical mechanisms on the CWRF bias reduction

This section explores the physical mechanisms through which NCP eliminated the warm and dry biases in CUS. The previous section compared the results from the three major changes to the ECP cumulus parameterization (CTL)—the Tokioka constraint, the JS trigger, and C0T autoconversion—separately as well as their total effects (NCP). We showed that the resulting temperature and precipitation changes had complex relationships with cloud, radiation, and other fields. The effects were neither local nor linear. It is thus challenging to gain physical insights from local and isolated comparisons. Below we performed two decomposition analyses to address the issues from the surface radiation budget and atmospheric diabatic cooling perspectives in the coupled climate system. Since the Tokioka constraint was built directly into the JS trigger as an additional limiting condition for convection to occur and produced some compensating results, we focused on their combined effects (JST).

a. Effects of the JS trigger and Tokioka constraint

Figure 6 compares the composite vertical profiles (cloud fraction and base/top pressure frequency, convective temperature, and water vapor tendencies) and relative differences due

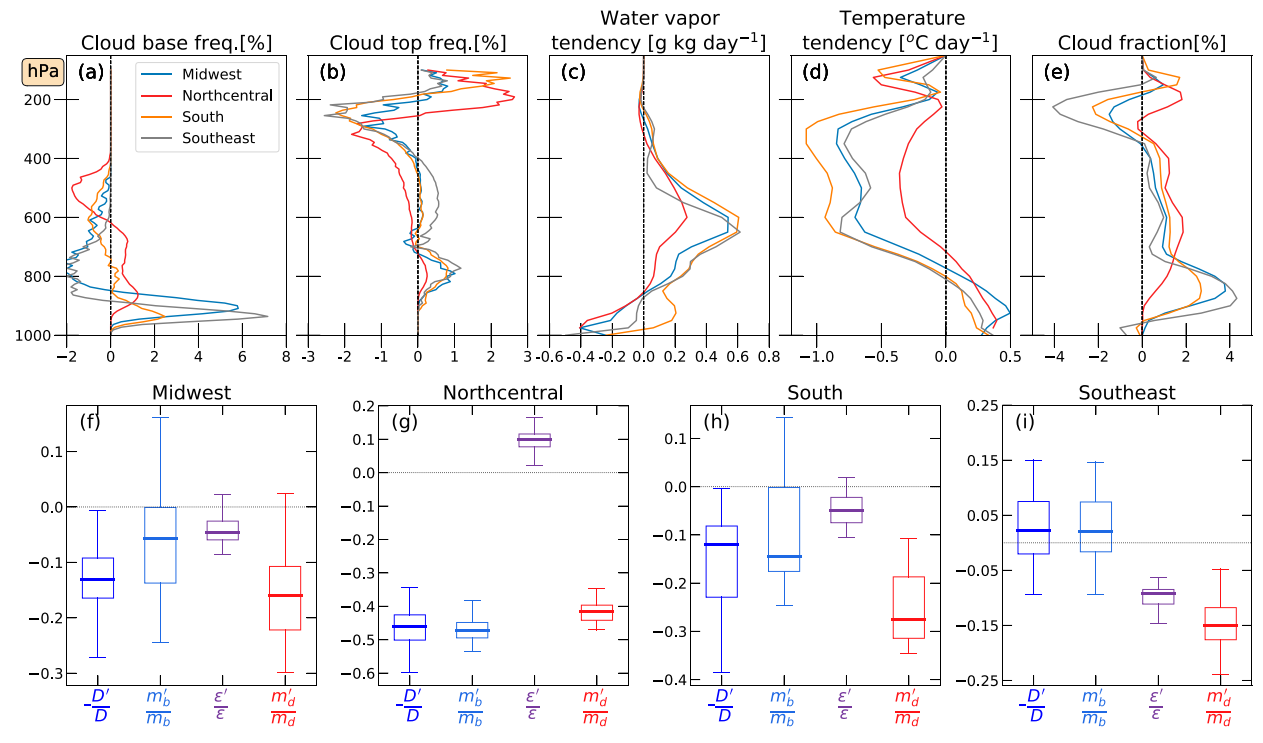


Fig. 6. Summer composite JST minus CTL changes over the four key regions (Midwest, North-Central, South, Southeast) separated by (a)–(e) colors and (f)–(i) titles. (a)–(e) The changes in the vertical profiles of the (a) cloud-base and (b) cloud-top pressure frequency, the convective (c) temperature (°C day⁻¹) and (d) water vapor (g kg⁻¹ day⁻¹) tendency, and (e) the cloud fraction (%). (f)–(i) The relative changes in the cumulus characteristic terms (F'/F), where the prime denotes for the change, and F for any feature among cloud pressure depth (D), cloud-base mass flux (m_b), downdraft mass flux (m_d), and $\varepsilon = m_d/m_b$.

to incorporating the JS trigger plus the Tokioka constraint (i.e., JST minus CTL). The composite was done on all grids over each of the four key regions when convections took place. The JST simulated systematically much lower cloud bases than CTL (Fig. 6a and Fig. S6), mainly because the JS trigger defines the cloud base at LCL that is generally lower than LFC. The CTL used LFC, which caused a systematic overestimation of cloud-base heights. Besides, the CTL cloud-base frequency had a pronounced zigzag distribution, while the JST profile was quite smooth (Fig. S6). This is because CTL using the default ECP located the cloud base simply at the discrete model level of LFC, while JST adopting the JS trigger located that at the closest model level to the exact pressure of LCL (Jakob and Siebesma 2003).

The composite analysis also shows that JST simulated systematically higher cloud tops than CTL (Fig. 6b). Thus, on average, coincident with a lower cloud base was a deeper cloud depth in the Midwest, North-Central, and South, albeit a slightly shallower depth in the Southeast (Fig. 6i). A cloud-base change may have important consequences on other cumulus characteristics, such as the downdraft mass flux (m_d) that determines convective effects on large-scale environments (Grell et al. 1994). To the first-order approximation (see appendix B for the derivation), the relative change in m_d can be estimated by the negative relative change in cloud pressure depth (D) and in the downdraft over (updraft)

cloud-base mass flux ratio (ε), $m'_d/m_d \approx -D'_d/D_d + \varepsilon'/\varepsilon$ [Eq. (B5)], where χ' denotes the change in χ . In addition, the relative change in cloud-base mass flux is approximately in proportion to the negative relative change in cloud depth, $m_b'/m_b \propto -D'/D$ [Eq. (B4)]. These approximations explain the composite analysis finding that in most regions a deeper convection [first term in Eq. (B5)] was identified with a weaker cloud-base mass flux [Eq. (B4)] hence a weaker downdraft, while in the Southeast the relative reduction of the mass flux ratio [second term in Eq. (B5)] dominated that of downdraft. This ratio reduction resulted from less in-cloud condensation by a thinner cloud and higher precipitation efficiency accompanying a lower cloud base (see the supplemental material for details). Overall, the above mechanism explains why the JS trigger, defining the cloud base at LCL rather than the higher level LFC, systematically simulated weaker downdrafts in all four regions. The reduced downdrafts caused weaker convective drying and warming in the mid- to upper layers (Figs. 6c,d), and consequently resulted in more low- to midlevel clouds (Fig. 6e), which reduced CTL cloud and radiation biases (Figs. 4 and 5).

The North-Central differs from other three regions in that its mass flux ratio (ε) was enhanced by JST, causing a weaker reduction in the downdraft than updraft. It was also identified with a much wider peak of the cloud-base frequency between 850 and 650 hPa than other regions, each with a distinct narrow peak around 900 hPa. The changes in the North-Central

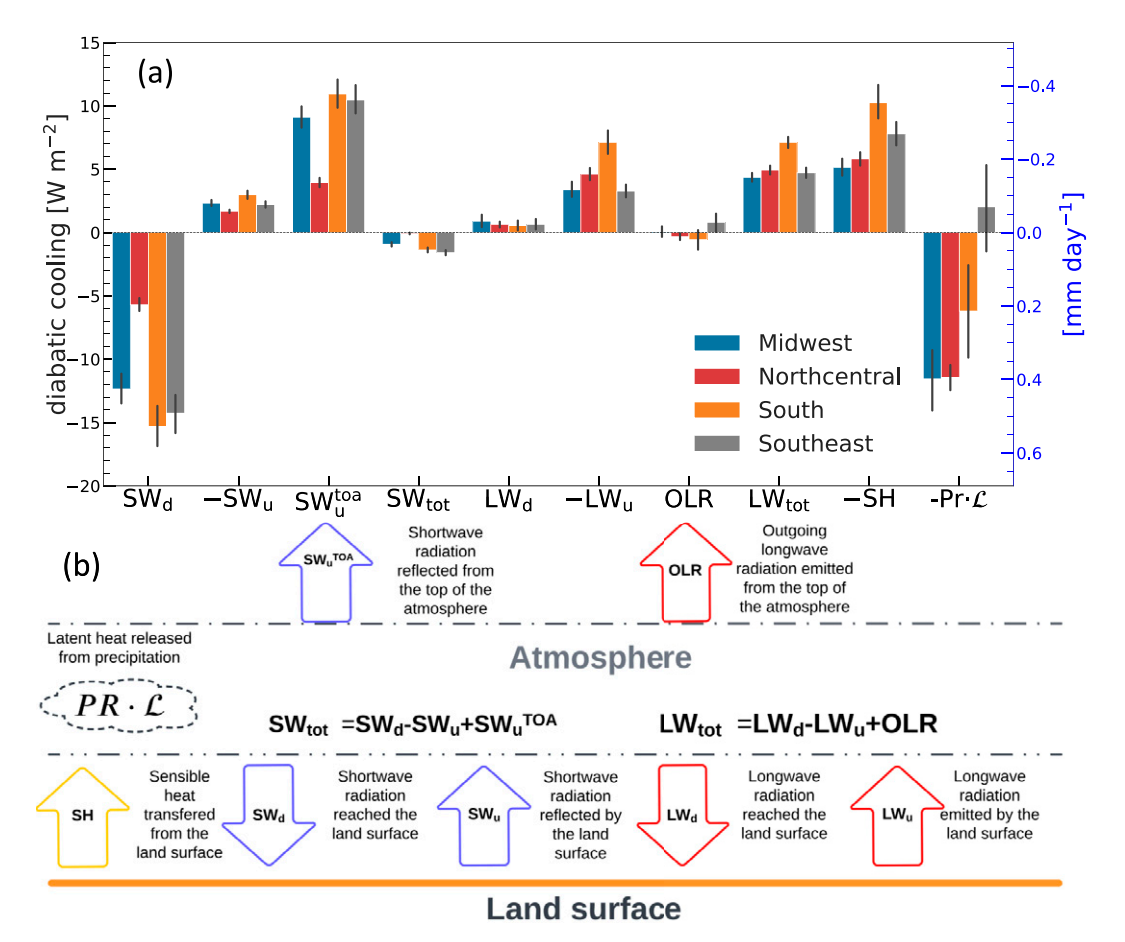


FIG. 7. (a) The summer mean JST minus CTL diabatic cooling changes as decomposed into the contributions from the surface downwelling and negative upwelling shortwave $(SW_d, -SW_d)$ and longwave $(LW_d, -LW_d)$ radiation, the top-of-the-atmosphere outgoing shortwave (SW_{tot}) and longwave (OLR) radiation, and their total $(SW_{tot} = SW_d - SW_u^{toa}, LW_{tot} = LW_d - LW_u + OLR)$, as well as the negative surface sensible heat (-SH) and the negative precipitation latent heat release $(-PR \cdot \mathcal{L})$. They are averaged during 1980–2019 over all grids with convections in the four key regions. The right y axis shows the equivalent precipitation units (mm day $^{-1}$), positive downward (e.g., JST simulated more precipitation in the Midwest). Black lines represent the 95% confidence interval estimated by the bootstrapping method of Linnet (2000) with 1000 resamples. (b) The meaning of each term.

were more evident for the increased midlevel clouds, but relatively small in the low- and high-level clouds. In contrast, the Midwest, South, and Southeast were all evident with significantly increased low and reduced high clouds. This contrast is likely because the precipitable water is much less abundant in the North-Central, inadequate to support deep convections. Therefore, it was not the cloud-induced shortwave biases, but the water vapor induced longwave biases, that dominated the warm biases in the North-Central (Figs. 2 and 4).

Figure 7 compares the atmospheric diabatic cooling compositions associated with the latent heat released due to precipitation changes when switching the CTL to JST parameterization. Following Muller and O'Gorman (2011), the decomposition links the changes in precipitation with cloud radiative forcing from an energetic perspective (ignoring the energy exchange outside the analysis region). The JST simulated large precipitation increases from CTL in the Midwest, North-Central, and South, but small

reductions in the Southeast. On average, the surface sensible heat reduction (more diabatic cooling) contributed the most to support more precipitation latent heat release, while the surface longwave emission reduction (again more diabatic cooling) played a secondary role. In all cases, the atmospheric total (surface downwelling minus top upwelling, i.e., SWtot in Fig. 7) shortwave adiabatic cooling changed little between JST and CTL, while the surface insolation reduction (SW_d) was canceled by the atmospheric top reflection (SW_u^{toa}). As explained earlier, JST simulated more low- to midlevel clouds, which initially reduced the surface insolation and ground skin temperature. Overall Fig. 7 implies the decrease in SH plus the decrease in LW approximated the increase in heat release due to precipitation. Physically, a cooler ground produced less sensible heat and longwave emission, both of which provided stronger diabatic cooling to balance more condensation heating and consequently increased precipitation (Eltahir 1998). S&L offered a more detailed

TABLE 3. The variance of the JST minus CTL changes in precipitation (PR) and temperature (T_2) that can be explained by the key diabatic cooling terms (LW_u + SH, SW_d, PR) and a combined regression (SW_d, PR). It is shown as the coefficient of determinant R^2 using 40 data samples and identified as statistically significant at the confidence level of 95% (*) or 99% (**).

		Region			
	Variable	Midwest	North- Central	South	Southeast
PR	$LW_u + SH$	0.62**	0.42**	0.80**	0.67**
T_2	SW_d	0.15*	0.41**	0.47**	0.48**
	PR	0.45**	0.31**	0.72**	0.48**
	Regression (SW_d, PR)	0.45**	0.50**	0.75**	0.54**

physical explanation on how diabatic cooling differences affect precipitation biases.

One exception was in the Southeast, where a large increase in the diabatic cooling from less surface sensible heat and longwave emission accompanied a small reduction in precipitation (Fig. 7). The long-term average may mask important relationships as complicated by other feedbacks. Hence, a linear regression was made between the composite changes in precipitation and the sum of two dominant diabatic cooling terms, that is, surface sensible heat plus longwave emission, from all individual years (Table 3). Strong positive correlations occurred in the Midwest, South, and Southeast, where the surface diabatic cooling changes explained the precipitation interannual differences between JST and CTL by, respectively, 62%, 80%, and 67% of the total variance. Now, the North-Central became exceptional, with the variance explained by only 42%. As discussed earlier, the North-Central is unique with more evident increases in mid-rather than low-level clouds. Together with terrain-induced precipitation anomalies, these bias characteristics may indicate different feedback

mechanisms in North-Central. On the other hand, the regression intercepts in the South and Southeast were much larger, indicating an important systematic contribution from the dry-static energy flux divergence missed in the long-term average. Nevertheless, through interactions with land surface processes, low- to midlevel cloud increases induced by deeper convections significantly reduced the warm and dry biases and strongly controlled precipitation interannual variations.

Interannual temperature differences between JST and CTL in the four regions (Midwest, North-Central, South, Southeast) were correlated with those of both surface insolation (positive) and precipitation (negative), respectively explaining (15%, 41%, 47%, 48%) and (45%, 31%, 72%, 48%) of the total variance. Notice the relatively small correlation with insolation in the Midwest and with precipitation in the North-Central. In all four regions, a simple linear regression with both insolation and precipitation led to overall larger correlations, explaining most of the T_2 variance (45%, 50%, 75%, 54%). Thus, the JST induced insolation reduction and precipitation increase collaborated to significantly diminish the regional warm biases. The key mechanisms and physical processes underlying this bias reduction were elaborated in S&L.

b. Effects of the temperature-dependent autoconversion

Figure 6 shows that JST reduced high-level clouds from CTL, which is not beneficial to overestimation of OLR in CTL (Fig. S2). This motivated improving cirrus clouds associated with deep convections to counter back the JST-caused OLR errors. Figure 8 compares the composite vertical profiles (convective water vapor and temperature tendencies, cloud fraction) between C0T and CTL. Overall changes from CTL to C0T were similar for all fields among the four regions. Most notably, C0T simulated a wetter tendency (up to 0.5 g kg⁻¹ day⁻¹) in the upper troposphere between 300 and 150 hPa. Our

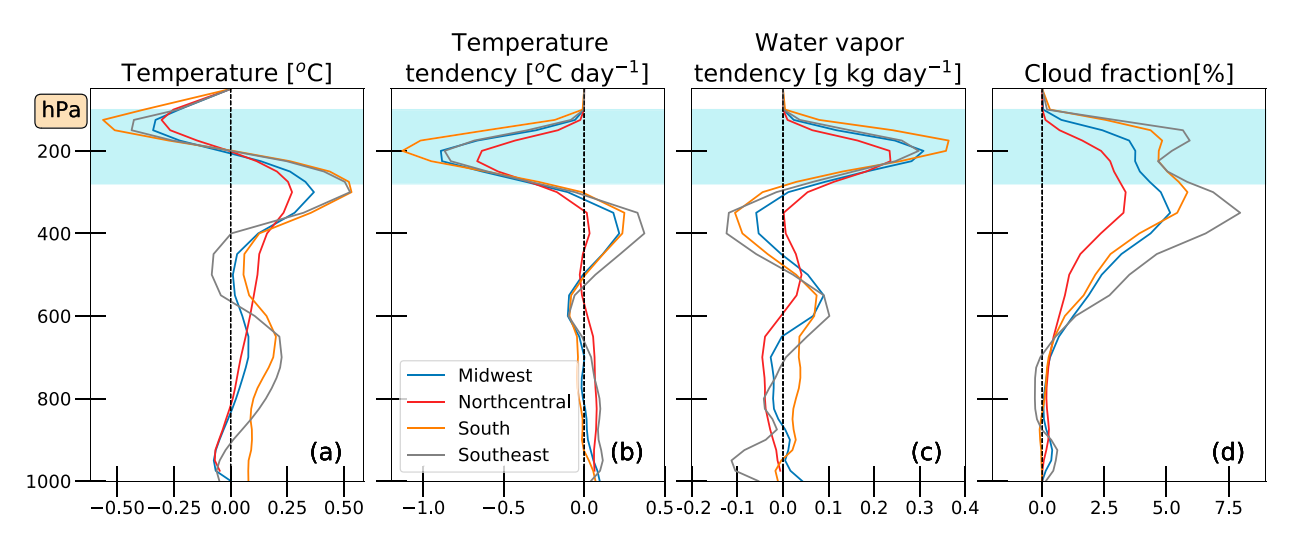


FIG. 8. Summer composite vertical profiles change (COT minus CTL) over the four key regions. (a) Temperature ($^{\circ}$ C), the convective tendency in (b) temperature ($^{\circ}$ C day $^{-1}$) and (c) water vapor (g kg $^{-1}$ day $^{-1}$), and (d) cloud fraction (%). The shaded area indicates where anvil cirrus occurs.

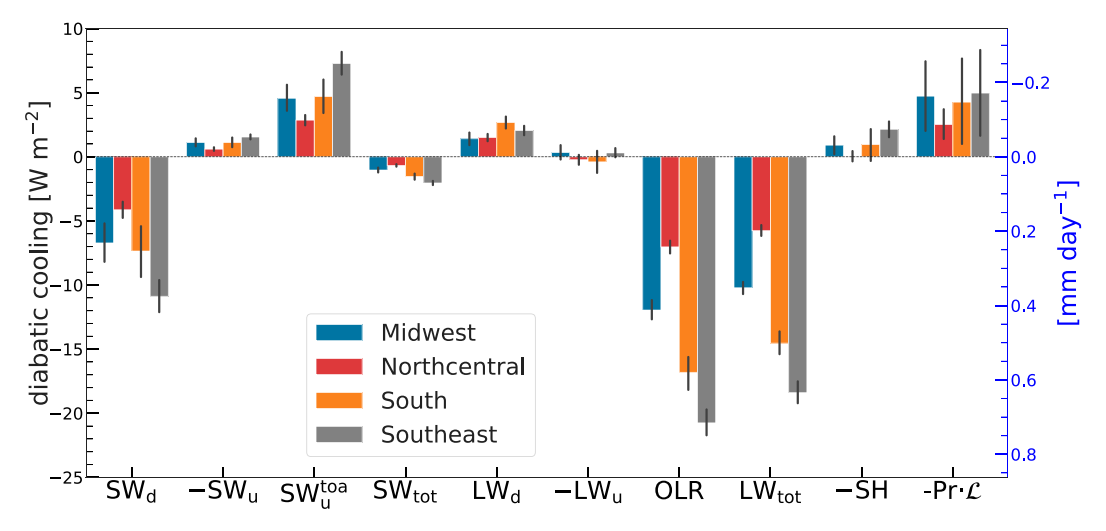


FIG. 9. As in Fig. 7a, but for COT minus CTL changes.

derivation in appendix A (A10) explains this positive anomaly in water vapor tendency was due to the vertical gradient of C_0 . A higher moisture tendency led to more cirrus clouds with less OLR, which caused a temperature decrease above the cloud and increase below. Thus, the environmental temperature change is a direct effect from the water vapor tendency perturbation. The enhanced vertical temperature gradient near the tropopause (\sim 200 hPa) reduced the upper tropospheric convective warming—an indirect effect of the water vapor tendency change. More cirrus led to larger warming at a higher altitude than near the surface and hence enhanced the column stability. Those extra water vapor near the tropopause subsided to further increase midlevel clouds.

As an additional benefit, COT produced a convective cold top, a prevalent mesoscale phenomenon observed in midlatitude summer (Fritsch and Brown 1982). To simulate this cold top in a Boussinesq model, the hydrostatic pressure perturbation created by the low-troposphere cumulus warming must be balanced by the pressure perturbation above (Holloway and Neelin 2007). Apparently, the CTL result shows that this balance is not warranted in a nonhydrostatic model. Instead, the indirect effect from the diabatic cooling due to cumulus turrets (anvil cirrus) offers a viable explanation. Both JST (Fig. 6) and COT (Fig. 8) captured this convective cold top.

Figure 9 compares the atmospheric diabatic cooling compositions associated with the latent heat released due to precipitation changes when switching the CTL to COT parameterization. In all four regions, COT produced systematically more cirrus clouds and so reduced OLR. On average, this OLR reduction dominated the total diabatic cooling change to allow less condensation heating and thus slightly less precipitation (with large uncertainty), which is consistent with the enhanced tropospheric stability (Fig. 8b). Both surface sensible heat increase and net shortwave radiation decrease were much smaller, while surface upwelling and atmospheric downwelling emission changes canceled each other. Hence, a linear regression was made between the interannual composite changes in precipitation and OLR (Table 4). Negative correlations were significant in the Midwest,

but became weaker in the North-Central, South, and Southeast where the OLR changes explained the precipitation interannual differences between C0T and CTL by, respectively, 44%, 12%, 22%, and 24% of the total variance. These relationships agreed with observations that correlations between OLR and precipitation were positive for the annual cycle but negative for interannual anomalies, depicting the relative roles of surface temperature and deep convection in the extratropics (Xie and Arkin 1998). On the other hand, the C0T induced insolation and precipitation changes still dominated surface temperature interannual differences, jointly explaining 54%, 53%, 82%, and 37% of the total variance.

Figure 10 summarizes the major physical processes and underlying mechanisms that explain how the new cumulus parameterization incorporating JST and C0T reduced the summer warm-and-dry biases in CUS. First, the JS trigger defines the cloud base at LCL, which reduces the cloud-base height and increases its depth. A deeper cloud reduces the mass flux at its base and so weakens its downdraft [Eq. (B5)], which decreases the convective drying and warming in the low- to midtroposphere and subsequently increases low to midlevel clouds (Fig. 6). Hence, less solar insolation reaches the surface so to cool the ground, which reduces sensible heat and longwave emission. This reduced surface forcing enhances the atmospheric diabatic cooling, which is associated with more condensation heating from heavier precipitation (Fig. 7).

TABLE 4. As in Table 3, but for COT minus CTL changes.

		Region			
	Variable	Midwest	North- Central	South	Southeast
PR T ₂	OLR PR Regression (SW _d , PR)	0.44** 0.50** 0.54**	0.12* 0.42** 0.53**	0.22** 0.68** 0.82**	0.24** 0.20** 0.37**

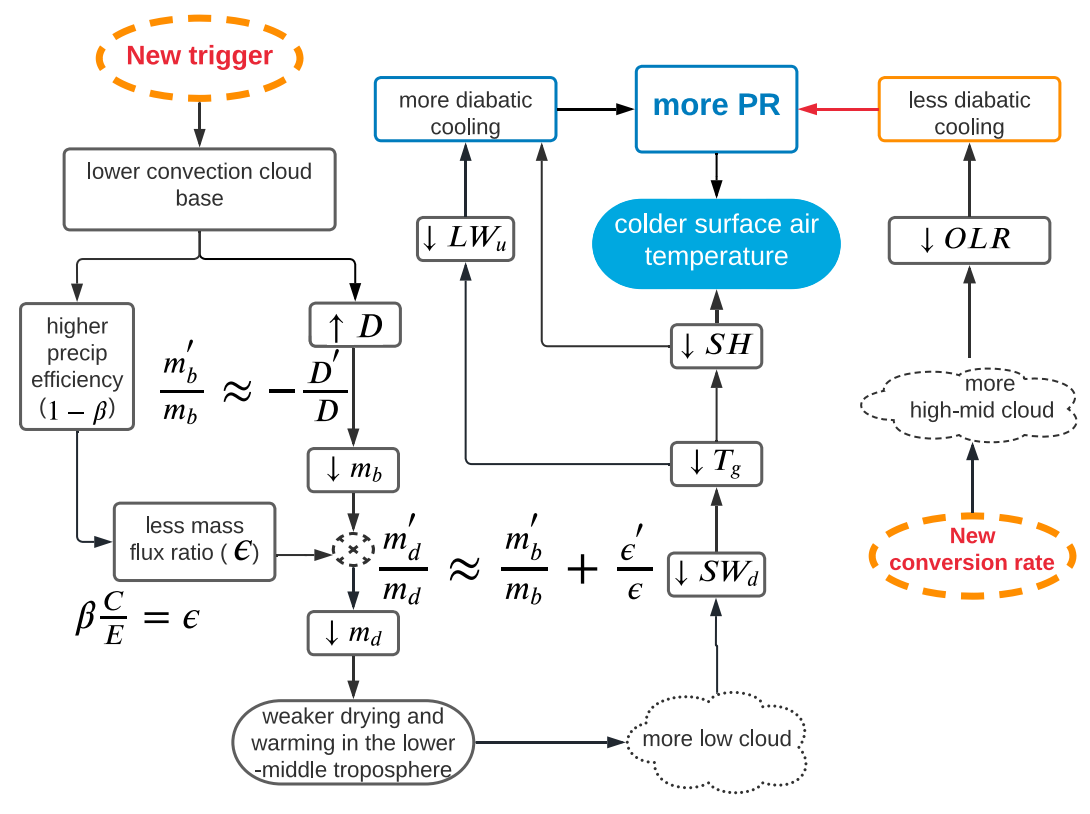


FIG. 10. The conceptual summary explaining the physics processes (pathways) through which the new cumulus parameterization (NCP) reduces the summer warm-and-dry biases in CUS. The upper-left and lower-right ovals represent, respectively, the NCP incorporation of the convection trigger function and cloud water-to-rain conversion rate, while the boxes are their corresponding physics processes. The black (red) arrows indicate the positive (negative) forcing.

Second, the Tokioka entrainment constraint prevents penetrative convection when the PBL is too shallow, which reduces the number of rainy days and total precipitation over warm oceans and coasts (Fig. 2 and Fig. S1). Third, the temperature dependence (and so vertical gradient) of the cloud-torainwater conversion rate produces a wetter upper troposphere and so more cirrus clouds (Fig. 8), which reduce OLR and thus the diabatic cooling to allow less condensation heating from lighter precipitation (Fig. 9). In all cases, any reduced insolation and/or increased precipitation result in a colder surface air temperature, although the strength of the responses depends on regions due to other feedbacks. S&L further elaborated the key feedback pathways involving both temperature and precipitation biases among CMIP models.

The CTL largely underestimated both low- and high-level clouds to cause substantial compensating errors between too much surface warming and too much OLR cooling (Fig. 2). On the other hand, JST simulated sufficient low-level clouds to significantly reduce the warm and dry biases in CUS. However, it still produced inadequate high-level clouds, breaking CTL's error compensation, to overestimate precipitation and OLR in broad regions around CUS (Fig. S2). Meanwhile, C0T systematically increased cirrus clouds and so reduced OLR. Together NCP (JST + C0T), through the robust physical mechanisms outlined above (Fig. 10), essentially eliminated the biases in CUS.

6. Summary and conclusions

This study aimed to use CWRF incorporating cumulus parameterization improvements to understand and reduce the long-lasting warm and dry summer biases in CUS that are common to global and regional climate models. The bias attribution and reduction are challenging because of the complex nonlinear land-atmosphere coupling feedbacks. To disentangle the complexity, we considered two unique summer climate features prevailing in CUS: convective activities under weak large-scale forcing conditions and cirrus clouds, both of which are associated with cumulus parameterization. We thus incorporated into CWRF ECP 1) the trigger function of Jakob and Siebesma (2003) to represent the lifting effect of small-scale rising motions associated with LLJ activities and midtropospheric perturbations to overcome CIN for MCS to occur in unfavorable environments, 2) the entrainment constraint of Tokioka et al. (1988) to prevent deep convection in case of shallow PBL to remedy the overestimation of precipitation frequency, and 3) the temperature-dependent cloud-torainwater conversion rate modified from Han et al. (2016) to increase water detrainment to form sufficient cirrus clouds. To facilitate the physical understanding, we conducted CWRF 1980-2019 simulations driven by ERA5 and decomposition analyses of the resulted surface radiation budget (Zhang et al. 2018; Van Weverberg et al. 2018) and precipitation heat budget (Muller and O'Gorman 2011). We found that the new ECP produced overall more realistic cloud amounts in both vertical distribution and optical depth, especially increased low- and high-level clouds, to largely reduce biases in the surface radiation budget and OLR, and through the robust physical mechanisms (Fig. 10) essentially eliminate CUS warm-and-dry biases.

Significant summer bias reductions from the new ECP also occurred in other key regions, including the Midwest, Southeast, Northeast, and the southern and eastern U.S. coastal oceans. In some regions and other seasons, a large room exists for further model improvements. In particular, pronounced biases in the western United States throughout the year involve different processes and need more detailed investigation. Nevertheless, the bias identification and process diagnosis procedures established in this study offer a practical guidance to detect the critical formulation deficiencies and understand the underlying physical mechanisms. For each region, it is vital to first identify the bias characteristics and their governing climate processes, and then detect the key model formulation deficiencies in representing these observed processes. Only after the signals are diagnosed and the processes understood can one develop and institute viable solutions to eliminate the regional biases in a physically consistent manner. Some of the findings from this study were applied in our companion paper S&L to identify the model deficiencies that may likely explain CUS warm and dry biases among CMIP models. We confirmed that the models defining the cloud base at LCL rather than LFC reduce the warm-and-dry biases and that the regional temperature and precipitation biases among all models are more generally explained by errors in surface shortwave insolation, longwave emission, and sensible heat. These results will be beneficial to seeking specific solutions based on individual models.

An important question is whether NCP improved precipitation diurnal cycle simulation. Figures S7 and S8 compare observed and CWRF simulated summer rainfall diurnal cycle in the eastward propagation for the 36°–42°N averaged amount and the geographical distribution of the phase or timing, respectively. The NCP showed noticeable improvement over CTL with an enhanced amplitude of the nocturnal precipitation across the Great Plains to Midwest, whereas the phase changed insignificantly. Improving the precipitation diurnal cycle warrants further investigation from both cumulus parameterization and convection-permitting modeling perspectives (Liang et al. 2004b; Gao et al. 2017).

Acknowledgments. The research was supported by the U.S. National Science Foundation Innovations at the Nexus of Food, Energy and Water Systems under Grant EAR1639327 and the U.S. Department of Agriculture–National Institute of Food and Agriculture under Grant 20206801231674 for developing the Dashboard for Agricultural Water use and Nutrient management at the University of Maryland and Grant 2015-34263-24070 for the UV-B Monitoring and Research Program at Colorado State University. The simulations and analyses were conducted on computers in the National Center for Atmospheric Research Computational and Information Systems

Lab and the Maryland Advanced Research Computing Center under Grant EES210017.

Data availability statement. All CWRF experiment outcomes used to generate the results in the manuscript are available from the corresponding author upon reasonable request.

APPENDIX A

Derivation of the Temperature-Dependent Cloud-to-Rain Autoconversion Effect

Following Grell et al. (1994),

$$\left[\frac{\partial h_e(z)}{\partial t} \right]_{\rm cu} = \frac{\partial h_e(z)}{\partial z} m_b (1 - \varepsilon) + \left[\frac{\partial h_u(z)}{\partial z} - \varepsilon \frac{\partial h_d(z)}{\partial z} \right] m_b \,, \tag{A1}$$

$$\left[\frac{\partial q_e(z)}{\partial t} \right]_{\rm cu} = \frac{\partial q_e(z)}{\partial z} m_b (1 - \varepsilon) + \left[\frac{\partial q_u(z)}{\partial z} - \varepsilon \frac{\partial q_d(z)}{\partial z} \right] m_b \,, \tag{A2}$$

$$h_u(z) = h_e(z_b) + h_s(z),$$
 (A3)

$$q_{\nu}(z) = q_{\varrho}(z_b) + q_{\varrho}(z), \tag{A4}$$

$$C_{p} \left[\frac{\partial T_{e}(z)}{\partial t} \right]_{CI} = \left[\frac{\partial h_{e}(z)}{\partial t} \right]_{CI} - L_{c} \left[\frac{\partial q_{e}(z)}{\partial t} \right]_{CI}, \tag{A5}$$

where q, h, and T are, respectively, moisture, moist static energy, and temperature, all depending on altitude (z). Subscript "cu" denotes the cumulus effect, e is an environmental variable, s is a source or sink, u is an updraft thermal, d is a downdraft, and b is cloud base. Other terms are as follows: m_b is the mass flux at the cloud base, C_p is the specific heat at a constant pressure, L_c the latent heat of condensation, and ε the mass flux ratio. Following Grell et al. (1994),

$$q_s = -C_0 m_b q_1, \tag{A6}$$

where q_1 is the cloud liquid water content and C_0 the cloud-to-rainwater conversion rate. Let us focus on the upper troposphere, where changing C_0 produced the largest difference in water vapor tendency (Fig. 8). Since the upper troposphere is above the downdraft originating level, all x_d terms are zeros. Substituting (A6) into (A4) and then (A2) yields

$$\begin{split} \left[\frac{\partial q_e(z)}{\partial t}\right]_{\rm cu} &= -\frac{\partial C_0(z)}{\partial z}q_{\rm l}m_b^2 - C_0(z)\frac{\partial q_{\rm l}(z)}{\partial z}m_b^2 + \frac{\partial q_e(z)}{\partial z}m_b(1-\varepsilon) \,. \end{split} \tag{A7}$$

In the C0T experiment, C_0 decreases with temperature, which is described as a sigmoid function,

$$C_0(z) = \begin{cases} \frac{a}{1 + \exp\left\{-[b + T(z)]\right\}} & \text{for } T(z) < T_0, \\ a & \text{for } T(z) > T_0, \end{cases}$$
(A8)

where $a = 0.002 \text{ m}^{-1}$ and $b = 39 - T_0 \text{ K}$ are tunable parameters, and $T_0 = 273.15 \text{ K}$ is the freezing point. In the upper troposphere $T(z) < T_0$, the ratio between first and second terms on the right side of Eq. (A7) is

$$\frac{\frac{\partial C_0(z)}{\partial z} q_1 m_b^2}{C_0(z) \frac{\partial q_1(z)}{\partial z} m_b^2} = \frac{\frac{-q_1}{[1 + e^{b + T_e(z)}]} \frac{\partial T_e(z)}{\partial z}}{\frac{\partial q_1(z)}{\partial z}}$$

$$\approx \frac{-q_1}{\frac{\partial q_1(z)}{\partial z}} \propto \mathcal{O}\left(\frac{QT}{\frac{Q}{Z}}\right) \propto \mathcal{O}(T) \gg 1. \quad (A9)$$

The above uses $1 + e^{b+T(z)} \approx 1$ and another scale approximation. Thus, we can neglect the second term in Eq. (A7). Assuming that the long-term mean environmental forcing remains approximately the same [the third term in Eq. (A7) is canceled], C0T replacing C00 (prescribed C_0 , $\partial C_0/\partial z = 0$) leads to

$$\begin{split} \left[\frac{\partial q_e(z)}{\partial t} \right]_{\text{cu}} &- \left[\frac{\partial q_e(z)}{\partial t} \right]_{\text{cu}} \right|_{\text{C00}} \approx -\frac{\partial C_0(z)}{\partial z} \ q_1 m_b^2 \\ &= \frac{a e^{-T_e(z) - b}}{[1 + e^{-T_e(z) - b}]^2} \ \frac{\partial T_e(z)}{\partial z} \ q_1 m_b^2. \end{split} \tag{A10}$$

Therefore, the vertical gradient of $C_0(z)$ [first term in Eq. (A7)] rather than its local value [second term in Eq. (A7)] dominates the C0T minus C00 difference in the cumulus effect on the environment water vapor tendency. As shown in Fig. S9, the magnitude of C_0 affects precipitation and temperature through its coefficient a [Eq. (A8)]. Reducing a by a factor of 5 decreased OLR by 10–25 W m⁻² and precipitation by 0.5–1.0 mm day⁻¹ in the Southeast, whereas increasing it by the same factor produced little effect. This factor change is extreme of the a's range, and in both extreme cases surface temperature changed insignificantly. In addition, the amplitude $\{ae^{-T_e(z)-b}/[1+e^{-T_e(z)-b}]^2\}$ in (A10) shows a "bumper" shape, which explains the profile of the water vapor tendency difference (Fig. 8).

Substituting Eqs. (A1) and (A2) into (A5), dropping downdraft terms as before, and using the moist static energy $h = C_pT + gz + L_cq$ yield

$$\begin{split} \left[\frac{\partial T_e(z)}{\partial t}\right]_{\text{cu}} &= \frac{m_b}{C_p} \frac{\partial}{\partial z} \{ [h_u - h_e(1-\varepsilon)] - L_c[q_u - q_e(1-\varepsilon)] \} \\ &= \frac{m_b}{C_p} \frac{\partial}{\partial z} [T_u - T_e(1-\varepsilon)]. \end{split} \tag{A11}$$

Thus, the contribution to $[\partial T_e(z)/\partial t]_{cu}$ from the vertical gradient of water vapor cancels that of the moist static energy. That is, the new C_0 scheme does not directly affect the temperature tendency through water vapor terms. Rather, the new scheme increases cirrus clouds, causing stronger radiative cooling above and warming below them, and hence enhances the large-scale temperature gradient near the tropopause. Finally, the new C_0 scheme reduced the cumulus temperature

tendency through the environmental temperature gradient in Eq. (A11).

APPENDIX B

Approximation of the Cloud Depth and Downdraft Mass-Flux Perturbation Relationship

Under the convective quasi equilibrium (Arakawa and Schubert 1974),

$$0 \approx \left(\frac{\partial A}{\partial t}\right)_{\text{total}} = \left(\frac{\partial A}{\partial t}\right)_{\text{LS}} + \left(\frac{\partial A}{\partial t}\right)_{\text{CU}},\tag{B1}$$

where the cloud-work function (A) change due to the largescale forcing (subscript LS) is balanced by that due to cumulus activities (subscript CU). Applying the chain rule and assuming initial mass flux at cloud base (m_b) is near zero.

$$\left(\frac{\partial A}{\partial t} \right)_{\rm LS} = - \left(\frac{\partial A}{\partial t} \right)_{\rm CU} = - \left(\frac{\partial A}{\partial m_b} \right)_{\rm CU} \frac{dm_b}{dt} \approx - \left(\frac{\partial A}{\partial m_b} \right)_{\rm CU} \frac{m_b}{\Delta t} \; .$$
 (B2)

Taking the linear approximation of Lord (1982), $A \approx A_N D$, where D denotes for the cumulus cloud depth and A_N the fitting coefficient. Assuming D changes mostly with m_b , the large-scale forcing (LSF) during a time period Δt is

$$\begin{split} \text{LSF} &\equiv \left(\frac{\partial A}{\partial t}\right)_{\text{LS}} \Delta t = -\left(\frac{\partial A}{\partial m_b}\right)_{\text{CU}} m_b \approx -A_N \; \frac{dD}{dm_b} m_b \Rightarrow d \; \ln(m_b) \\ &\approx -\frac{A_N}{\text{LSE}} \; dD. \end{split} \tag{B3}$$

Following Yano et al. (2000), the long-term mean environmental forcing is approximated as constant. For a small perturbation, Eq. (B3) yields $m_b'/m_b \approx -A_N D'/\text{LSF}$. Taking the scale approximation $\mathcal{O}(A_N/\text{LSF}) \sim \mathcal{O}[A_N/(A_N D)] \propto 1/D$ leads to

$$\frac{m_b'}{m_b} \approx -\frac{A_N \cdot D'}{\text{LSF}} \propto -\frac{D'}{D} \Rightarrow \frac{m_b'}{m_b} \propto -\frac{D'}{D}$$
 (B4)

Following Grell et al. (1994), the convective downdraft mass flux is proportional to the updraft base mass flux, $m_d = \varepsilon \cdot m_b$ or $\ln(m_d) - \ln(\varepsilon) = \ln(m_b)$. For a small perturbation,

$$\frac{m'_d}{m_d} - \frac{\varepsilon'}{\varepsilon} \approx \frac{m'_b}{m_b} \Rightarrow \frac{m'_d}{m_d} \propto -\frac{D'}{D} + \frac{\varepsilon'}{\varepsilon} \,. \tag{B5}$$

Thus, under the same large-scale forcing, the relative change in downdraft mass flux is proportional to that in the mass flux ratio minus that in the cloud depth, that is, a deeper cloud led to less downdraft.

REFERENCES

Abatzoglou, J. T., 2013: Development of gridded surface meteorological data for ecological applications and modelling. *Int. J. Climatol.*, **33**, 121–131, https://doi.org/10.1002/joc.3413.

- Arakawa, A., and W. H. Schubert, 1974: Interaction of a cumulus cloud ensemble with the large-scale environment, Part I. *J. Atmos. Sci.*, **31**, 674–701, https://doi.org/10.1175/1520-0469 (1974)031<0674:IOACCE>2.0.CO;2.
- Augustine, J. A., and F. Caracena, 1994: Lower-tropospheric precursors to nocturnal MCS development over the central United States. Wea. Forecasting, 9, 116–135, https://doi.org/10.1175/1520-0434(1994)009<0116:LTPTNM>2.0.CO;2.
- Bechtold, P., M. Köhler, T. Jung, F. Doblas-Reyes, M. Leutbecher, M. Rodwell, F. Vitart, and G. Balsamo, 2008: Advances in simulating atmospheric variability with the ECMWF model: From synoptic to decadal time-scales. *Quart. J. Roy. Meteor.* Soc., 134, 1337–1351, https://doi.org/10.1002/qj.289.
- Bodas-Salcedo, A., and Coauthors, 2011: COSP: Satellite simulation software for model assessment. *Bull. Amer. Meteor. Soc.*, **92**, 1023–1043, https://doi.org/10.1175/2011BAMS2856.1.
- Chasteen, M. B., S. E. Koch, and D. B. Parsons, 2019: Multiscale processes enabling the longevity and daytime persistence of a nocturnal mesoscale convective system. *Mon. Wea. Rev.*, 147, 733–761, https://doi.org/10.1175/MWR-D-18-0233.1.
- Cheruy, F., J. L. Dufresne, F. Hourdin, and A. Ducharne, 2014: Role of clouds and land-atmosphere coupling in midlatitude continental summer warm biases and climate change amplification in CMIP5 simulations. *Geophys. Res. Lett.*, 41, 6493– 6500, https://doi.org/10.1002/2014GL061145.
- Choi, H. I., and X.-Z. Liang, 2010: Improved terrestrial hydrologic representation in mesoscale land surface models. *J. Hydrometeor.*, 11, 797–809, https://doi.org/10.1175/2010JHM1221.1.
- ——, P. Kumar, and X.-Z. Liang, 2007: Three-dimensional volume-averaged soil moisture transport model with a scalable parameterization of subgrid topographic variability. *Water Resour. Res.*, 43, W04414, https://doi.org/10.1029/2006WR005134.
- ——, X.-Z. Liang, and P. Kumar, 2013: A conjunctive surface-subsurface flow representation for mesoscale land surface models. *J. Hydrometeor.*, 14, 1421–1442, https://doi.org/10.1175/JHM-D-12-0168.1.
- Dai, Y., and Coauthors, 2003: The Common Land Model. *Bull. Amer. Meteor. Soc.*, **84**, 1013–1024, https://doi.org/10.1175/BAMS-84-8-1013.
- —, R. E. Dickinson, and Y.-P. Wang, 2004: A two-big-leaf model for canopy temperature, photosynthesis, and stomatal conductance. *J. Climate*, 17, 2281–2299, https://doi.org/10.1175/1520-0442(2004)017<2281:ATMFCT>2.0.CO;2.
- Donner, L. J., 1993: A cumulus parameterization including mass fluxes, vertical momentum dynamics, and mesoscale effects. *J. Atmos. Sci.*, **50**, 889–906, https://doi.org/10.1175/1520-0469(1993)050<0889:ACPIMF>2.0.CO:2.
- Eltahir, E. A., 1998: A soil moisture–rainfall feedback mechanism: 1. Theory and observations. *Water Resour. Res.*, 34, 765–776, https://doi.org/10.1029/97WR03499.
- Emanuel, K. A., and M. Živković-Rothman, 1999: Development and evaluation of a convection scheme for use in climate models. *J. Atmos. Sci.*, **56**, 1766–1782, https://doi.org/10.1175/1520-0469(1999)056<1766:DAEOAC>2.0.CO;2.
- Evans, S., R. Marchand, T. Ackerman, L. Donner, J.-C. Golaz, and C. Seman, 2017: Diagnosing cloud biases in the GFDL AM3 model with atmospheric classification. J. Geophys. Res. Atmos., 122, 12 827–12 844, https://doi.org/10.1002/2017JD027163.
- Feng, Z., R. A. Houze Jr., L. R. Leung, F. Song, J. C. Hardin, J. Wang, W. I. Gustafson, and C. R. Homeyer, 2019: Spatiotemporal characteristics and large-scale environments of mesoscale convective systems east of the Rocky Mountains. *J. Climate*, 32, 7303–7328, https://doi.org/10.1175/JCLI-D-19-0137.1.

- —, F. Song, K. Sakaguchi, and L. R. Leung, 2021: Evaluation of mesoscale convective systems in climate simulations: Methodological development and results from MPAS-CAM over the United States. *J. Climate*, 34, 2611–2633, https://doi.org/10.1175/JCLI-D-20-0136.1.
- Fletcher, N. H., 1962: *The Physics of Rainclouds*. Cambridge University Press, 389 pp.
- Fowler, L. D., and D. A. Randall, 1994: A global radiative-convective feedback. *Geophys. Res. Lett.*, 21, 2035–2038, https://doi.org/10.1029/94GL01711.
- Fritsch, J. M., and J. M. Brown, 1982: On the generation of convectively driven mesohighs aloft. *Mon. Wea. Rev.*, **110**, 1554–1563, https://doi.org/10.1175/1520-0493(1982)110<1554:OTGOCD>2.
- Gan, Y., X.-Z. Liang, Q. Duan, H. I. Choi, Y. Dai, and H. Wu, 2015: Stepwise sensitivity analysis from qualitative to quantitative: Application to the terrestrial hydrological modeling of a Conjunctive Surface-Subsurface Process (CSSP) land surface model. J. Adv. Model. Earth Syst., 7, 648–669, https://doi. org/10.1002/2014MS000406.
- Gao, Y., L. R. Leung, C. Zhao, and S. Hagos, 2017: Sensitivity of US summer precipitation to model resolution and convective parameterizations across gray zone resolutions. *J. Geophys. Res.* Atmos., 122, 2714–2733, https://doi.org/10.1002/2016JD025896.
- Geerts, B., and Coauthors, 2017: The 2015 Plains Elevated Convection At Night field project. *Bull. Amer. Meteor. Soc.*, 98, 767–786, https://doi.org/10.1175/BAMS-D-15-00257.1.
- Goswami, T., P. Mukhopadhyay, M. Ganai, R. P. M. Krishna, M. Mahakur, and J.-Y. Han, 2020: How changing cloud water to rain conversion profile impacts on radiation and its linkage to a better Indian summer monsoon rainfall simulation. *Theor. Appl. Climatol.*, 141, 947–958, https://doi.org/10.1007/s00704-020-03222-3.
- Grell, G. A., and D. Dvénéyi, 2002: A generalized approach to parameterizing convection combining ensemble and data assimilation techniques. *Geophys. Res. Lett.*, 29, 1693, https:// doi.org/10.1029/2002GL015311.
- —, J. Dudhia, and D. R. Stauffer, 1994: A description of the fifth-generation Penn State/NCAR Mesoscale Model (MM5). NCAR Tech. Note NCAR/TN-398+STR, 121 pp., https://doi. org/10.5065/D60Z716B.
- Guo, Z., and Coauthors, 2006: GLACE: The Global Land–Atmosphere Coupling Experiment. Part II: Analysis. J. Hydrometeor., 7, 611–625, https://doi.org/10.1175/JHM511.1.
- Gupta, S. K., N. A. Ritchey, A. C. Wilber, C. H. Whitlock, G. G. Gibson, and P. W. Stackhouse, 1999: A climatology of surface radiation budget derived from satellite data. *J. Climate*, 12, 2691–2710, https://doi.org/10.1175/1520-0442(1999)012 <2691:ACOSRB>2.0.CO;2.
- Han, J., W. Wang, Y. C. Kwon, S.-Y. Hong, V. Tallapragada, and F. Yang, 2017: Updates in the NCEP GFS cumulus convection schemes with scale and aerosol awareness. *Wea. Forecasting*, 32, 2005–2017, https://doi.org/10.1175/WAF-D-17-0046.1.
- Han, J.-Y., S.-Y. Hong, K.-S. S. Lim, and J. Han, 2016: Sensitivity of a cumulus parameterization scheme to precipitation production representation and its impact on a heavy rain event over Korea. *Mon. Wea. Rev.*, **144**, 2125–2135, https://doi.org/ 10.1175/MWR-D-15-0255.1.
- Hartmann, D. L., J. R. Holton, and Q. Fu, 2001: The heat balance of the tropical tropopause, cirrus, and stratospheric dehydration. *Geophys. Res. Lett.*, 28, 1969–1972, https://doi.org/10.1029/ 2000GL012833.

- Hersbach, H., and Coauthors, 2020: The ERA5 global reanalysis. *Quart. J. Roy. Meteor. Soc.*, **146**, 1999–2049, https://doi.org/10.1002/qj.3803.
- Holloway, C. E., and J. D. Neelin, 2007: The convective cold top and quasi equilibrium. J. Atmos. Sci., 64, 1467–1487, https:// doi.org/10.1175/JAS3907.1.
- Holtslag, A. A. M., and B. A. Boville, 1993: Local versus nonlocal boundary-layer diffusion in a global climate model. *J. Cli-mate*, 6, 1825–1842, https://doi.org/10.1175/1520-0442(1993) 006<1825:LVNBLD>2.0.CO;2.
- Hong, S.-Y., and H.-L. Pan, 1998: Convective trigger function for a mass-flux cumulus parameterization scheme. *Mon. Wea. Rev.*, **126**, 2599–2620, https://doi.org/10.1175/1520-0493(1998) 126<2599:CTFFAM>2.0.CO;2.
- Hu, H., L. R. Leung, and Z. Feng, 2020: Observed warm-season characteristics of MCS and non-MCS rainfall and their recent changes in the central United States. *Geophys. Res. Lett.*, 47, e2019GL086783, https://doi.org/10.1029/2019GL086783.
- —, and —, 2021: Early warm-season mesoscale convective systems dominate soil moisture–precipitation feedback for summer rainfall in central United States. *Proc. Natl. Acad. Sci. USA*, **118**, e2105260118, https://doi.org/10.1073/pnas.2105260118.
- Jakob, C., and A. P. Siebesma, 2003: A new subcloud model for mass-flux convection schemes: Influence on triggering, updraft properties, and model climate. *Mon. Wea. Rev.*, 131, 2765–2778, https://doi.org/10.1175/1520-0493(2003)131<2765: ANSMFM>2.0.CO;2.
- Ji, P., X. Yuan, and X.-Z. Liang, 2017: Do lateral flows matter for the hyperresolution land surface modeling? J. Geophys. Res. Atmos., 122, 12 077–12 092, https://doi.org/10.1002/2017JD027366.
- Jiang, R., L. Sun, C. Sun, and X.-Z. Liang, 2021: CWRF down-scaling and understanding of China precipitation projections. Climate Dyn., 57, 1079–1096, https://doi.org/10.1007/s00382-021-05759-z.
- Johns, R. H., 1993: Meteorological conditions associated with bow echo development in convective storms. Wea. Forecasting, 8, 294–299, https://doi.org/10.1175/1520-0434(1993)008<0294: MCAWBE>2.0.CO;2.
- Joos, H., P. Spichtinger, U. Lohmann, J.-F. Gayet, and A. Minikin, 2008: Orographic cirrus in the global climate model ECHAM5. J. Geophys. Res., 113, D18205, https://doi.org/10. 1029/2007JD009605.
- Kay, J. E., and Coauthors, 2012: Exposing global cloud biases in the Community Atmosphere Model (CAM) using satellite observations and their corresponding instrument simulators. *J. Climate*, 25, 5190–5207, https://doi.org/10.1175/JCLI-D-11-00469.1.
- Klein, S. A., X. Jiang, J. Boyle, S. Malyshev, and S. Xie, 2006: Diagnosis of the summertime warm and dry bias over the US Southern Great Plains in the GFDL climate model using a weather forecasting approach. *Geophys. Res. Lett.*, 33, L18805, https://doi.org/10.1029/2006GL027567.
- Kollias, P., G. Tselioudis, and B. A. Albrecht, 2007: Cloud climatology at the Southern Great Plains and the layer structure, drizzle, and atmospheric modes of continental stratus. *J. Geophys. Res.*, 112, D09116, https://doi.org/10.1029/2006JD007307.
- Li, Q., T. Wang, F. Wang, X.-Z. Liang, C. Zhao, L. Dong, C. Zhao, and B. Xie, 2021: Dynamical downscaling simulation of the East Asian summer monsoon in a regional Climate-Weather Research and Forecasting Model. *Int. J. Climatol.*, 41, E1700–E1716, https://doi.org/10.1002/joc.6800.

- Liang, X.-Z., L. Li, K. E. Kunkel, M. Ting, and J. X. L. Wang, 2004a: Regional climate model simulation of U.S. precipitation during 1982–2002. Part I: Annual cycle. J. Climate, 17, 3510–3529, https://doi.org/10.1175/1520-0442(2004)017<3510: RCMSOU>2.0.CO;2.
- —, —, A. Dai, and K. E. Kunkel, 2004b: Regional climate model simulation of summer precipitation diurnal cycle over the United States. *Geophys. Res. Lett.*, 31, L24208, https://doi. org/10.1029/2004GL021054.
- —, and Coauthors, 2005a: Development of land surface albedo parameterization based on Moderate Resolution Imaging Spectroradiometer (MODIS) data. *J. Geophys. Res.*, 110, D11107, https://doi.org/10.1029/2004JD005579.
- ——, H. I. Choi, K. E. Kunkel, Y. Dai, E. Joseph, J. X. L. Wang, and P. Kumar, 2005b: Surface boundary conditions for mesoscale regional climate models. *Earth Interact.*, 9, https://doi.org/10.1175/EI151.1.
- —, and Coauthors, 2012: Regional Climate–Weather Research and Forecasting Model. *Bull. Amer. Meteor. Soc.*, 93, 1363– 1387, https://doi.org/10.1175/BAMS-D-11-00180.1.
- —, and Coauthors, 2019: CWRF performance at downscaling China climate characteristics. *Climate Dyn.*, **52**, 2159–2184, https://doi.org/10.1007/s00382-018-4257-5.
- Lim, K.-S. S., and Coauthors, 2014: Investigation of aerosol indirect effects using a cumulus microphysics parameterization in a regional climate model. *J. Geophys. Res. Atmos.*, 119, 906–926, https://doi.org/10.1002/2013JD020958.
- Lin, Y., and K. E. Mitchell, 2005: The NCEP stage II/IV hourly precipitation analyses: Development and applications. *Proc. 19th Conf. on Hydrology*, San Diego, CA, Amer. Meteor. Soc., 1.2, https://ams.confex.com/ams/Annual2005/techprogram/paper_83847.htm.
- —, W. Dong, M. Zhang, Y. Xie, W. Xue, J. Huang, and Y. Luo, 2017: Causes of model dry and warm bias over central US and impact on climate projections. *Nat. Commun.*, 8, 881, https://doi.org/10.1038/s41467-017-01040-2.
- Linnet, K., 2000: Nonparametric estimation of reference intervals by simple and bootstrap-based procedures. *Clin. Chem.*, 46, 867–869, https://doi.org/10.1093/clinchem/46.6.867.
- Lord, S. J., 1982: Interaction of a cumulus cloud ensemble with the large-scale environment. Part III: Semi-prognostic test of the Arakawa-Schubert cumulus parameterization. *J. Atmos. Sci.*, **39**, 88–103, https://doi.org/10.1175/1520-0469(1982)039 <0088:IOACCE>2.0.CO;2.
- Ma, H.-Y., and Coauthors, 2018: CAUSES: On the role of surface energy budget errors to the warm surface air temperature error over the central United States. *J. Geophys. Res. Atmos.*, 123, 2888–2909, https://doi.org/10.1002/2017JD027194.
- Marsham, J. H., P. Knippertz, N. S. Dixon, D. J. Parker, and G. M. S. Lister, 2011: The importance of the representation of deep convection for modeled dust-generating winds over West Africa during summer. *Geophys. Res. Lett.*, 38, L16803, https://doi.org/10.1029/2011GL048368.
- Mesinger, F., and Coauthors, 2006: North American Regional Reanalysis. *Bull. Amer. Meteor. Soc.*, 87, 343–360, https://doi.org/10.1175/BAMS-87-3-343.
- Moore, J. T., F. H. Glass, C. E. Graves, S. M. Rochette, and M. J. Singer, 2003: The environment of warm-season elevated thunderstorms associated with heavy rainfall over the central United States. Wea. Forecasting, 18, 861–878, https://doi.org/10.1175/1520-0434(2003)018<0861:TEOWET>2.0.CO;2.

- Morcrette, C. J., and Coauthors, 2018: Introduction to CAUSES: Description of weather and climate models and their near-surface temperature errors in 5 day hindcasts near the Southern Great Plains. *J. Geophys. Res. Atmos.*, **123**, 2655–2683, https://doi.org/10.1002/2017JD027199.
- Mueller, B., and S. I. Seneviratne, 2014: Systematic land climate and evapotranspiration biases in CMIP5 simulations. Geophys. Res. Lett., 41, 128–134, https://doi.org/10.1002/2013GL058055.
- Muller, C. J., and P. A. O'Gorman, 2011: An energetic perspective on the regional response of precipitation to climate change. *Nat. Climate Change*, 1, 266–271, https://doi.org/10.1038/nclimate1169.
- Parish, T. R., R. D. Clark, and T. D. Sikora, 2020: Nocturnal destabilization associated with the summertime Great Plains low-level jet. *Mon. Wea. Rev.*, 148, 4641–4656, https://doi.org/10.1175/MWR-D-19-0394.1.
- Park, S., and C. S. Bretherton, 2009: The University of Washington shallow convection and moist turbulence schemes and their impact on climate simulations with the Community Atmosphere Model. J. Climate, 22, 3449–3469, https://doi.org/10.1175/2008JCLI2557.1.
- Platnick, S., and Coauthors, 2015: MODIS cloud optical properties: User guide for the Collection 6 level-2 MOD06/MYD06 product and associated level-3 datasets, version 1.0. NASA GSFC Doc., 145 pp., https://modis-images.gsfc.nasa.gov/_docs/C6MOD06OPUserGuide.pdf.
- Pokharel, B., S.-Y. S. Wang, J. Meyer, R. Gillies, and Y.-H. Lin, 2019: Climate of the weakly-forced yet high-impact convective storms throughout the Ohio River valley and mid-Atlantic United States. Climate Dyn., 52, 5709–5721, https://doi.org/10. 1007/s00382-018-4472-0.
- Qiao, F., and X.-Z. Liang, 2015: Effects of cumulus parameterizations on predictions of summer flood in the central United States. *Climate Dyn.*, 45, 727–744, https://doi.org/10.1007/s00382-014-2301-7.
- —, and —, 2016: Effects of cumulus parameterization closures on simulations of summer precipitation over the United States coastal oceans. *J. Adv. Model. Earth Syst.*, 8, 764–785, https://doi.org/10.1002/2015MS000621.
- —, and —, 2017: Effects of cumulus parameterization closures on simulations of summer precipitation over the continental United States. *Climate Dyn.*, **49**, 225–247, https://doi.org/10.1007/s00382-016-3338-6.
- Song, F., Z. Feng, L. R. Leung, R. A. Houze Jr., J. Wang, J. Hardin, and C. R. Homeyer, 2019: Contrasting spring and summer large-scale environments associated with mesoscale convective systems over the U.S. Great Plains. *J. Climate*, 32, 6749–6767, https://doi.org/10.1175/JCLI-D-18-0839.1.
- Stensrud, D. J., and J. M. Fritsch, 1994: Mesoscale convective systems in weakly forced large-scale environments. Part II: Generation of a mesoscale initial condition. *Mon. Wea. Rev.*, 122, 2068–2083, https://doi.org/10.1175/1520-0493(1994)122<2068: MCSIWF>2.0.CO;2.
- Sun, C., and X.-Z. Liang, 2020a: Improving US extreme precipitation simulation: Sensitivity to physics parameterizations. *Climate Dyn.*, 54, 4891–4918, https://doi.org/10.1007/s00382-020-05267-6.
- —, and —, 2020b: Improving US extreme precipitation simulation: Dependence on cumulus parameterization and underlying mechanism. *Climate Dyn.*, **55**, 1325–1352, https://doi.org/10.1007/s00382-020-05328-w.

- —, and —, 2023: Understanding and reducing warm and dry summer biases in the central United States: Analytical modeling to identify the mechanisms for CMIP ensemble error spread. *J. Climate*, 36, 2035–2054, https://doi.org/10.1175/ JCLI-D-22-0255.1.
- Swales, D. J., R. Pincus, and A. Bodas-Salcedo, 2018: The Cloud Feedback Model Intercomparison Project Observational Simulator Package: Version 2. *Geosci. Model Dev.*, 11, 77–81, https://doi.org/10.5194/gmd-11-77-2018.
- Tiedtke, M., 1983: The sensitivity of the time-mean large-scale flow to cumulus convection in the ECMWF model. *Proc. ECMWF Workshop on Convection in Large-Scale Models*, Reading, United Kingdom, ECMWF, 297–316, https://www.ecmwf.int/node/12733.
- Tokioka, T., K. Yamazaki, A. Kitoh, and T. Ose, 1988: The equatorial 30-60 day oscillation and the Arakawa-Schubert penetrative cumulus parameterization. *J. Meteor. Soc. Japan*, 66, 883–901, https://doi.org/10.2151/jmsj1965.66.6.883.
- Troen, I. B., and L. Mahrt, 1986: A simple model of the atmospheric boundary layer; sensitivity to surface evaporation. Bound.-Layer Meteor., 37, 129–148, https://doi.org/10.1007/BF00122760.
- Tselioudis, G., W. B. Rossow, C. Jakob, J. Remillard, D. Tropf, and Y. Zhang, 2021: Evaluation of clouds, radiation, and precipitation in CMIP6 models using global weather states derived from ISCCP-H cloud property data. *J. Climate*, 34, 7311–7324, https://doi.org/10.1175/JCLI-D-21-0076.1.
- Van Weverberg, K., and Coauthors, 2018: CAUSES: Attribution of surface radiation biases in NWP and climate models near the US Southern Great Plains. J. Geophys. Res. Atmos., 123, 3612–3644, https://doi.org/10.1002/2017JD027188.
- Wang, S.-Y., and A. J. Clark, 2010: NAM model forecasts of warm-season quasi-stationary frontal environments in the central United States. Wea. Forecasting, 25, 1281–1292, https://doi.org/10.1175/2010WAF2222394.1.
- —, T.-C. Chen, and S. E. Taylor, 2009: Evaluations of NAM forecasts on midtropospheric perturbation-induced convective storms over the U.S. northern plains. *Wea. Forecasting*, 24, 1309–1333, https://doi.org/10.1175/2009WAF2222185.1.
- —, and J. Correia, 2011: Climatology of summer midtropospheric perturbations in the US northern plains. Part I: Influence on northwest flow severe weather outbreaks. Climate Dyn., 36, 793–810, https://doi.org/10.1007/s00382-009-0696-3.
- Xie, P., and P. A. Arkin, 1998: Global monthly precipitation estimates from satellite-observed outgoing longwave radiation. *J. Climate*, 11, 137–164, https://doi.org/10.1175/1520-0442(1998) 011<0137:GMPEFS>2.0.CO;2.
- Xu, M., X.-Z. Liang, A. Samel, and W. Gao, 2014: MODIS consistent vegetation parameter specifications and their impacts on regional climate simulations. *J. Climate*, 27, 8578–8596, https://doi.org/10.1175/JCLI-D-14-00082.1.
- Yano, J.-I., G. L. Roff, W. W. Grabowski, and B. E. Mapes, 2000: Asymptotic approaches to convective quasi-equilibrium. *Quart. J. Roy. Meteor. Soc.*, 126, 1861–1887, https://doi.org/10.1002/qj. 49712656615.
- Yuan, X., and X.-Z. Liang, 2011: Evaluation of a Conjunctive Surface–Subsurface Process model (CSSP) over the contiguous United States at regional–local scales. *J. Hydrometeor.*, 12, 579–599, https://doi.org/10.1175/2010JHM1302.1.
- Zhang, C., and Y. Wang, 2017: Projected future changes of tropical cyclone activity over the western North and South Pacific

- in a 20-km-mesh regional climate model. *J. Climate*, **30**, 5923–5941, https://doi.org/10.1175/JCLI-D-16-0597.1.
- —, S. Xie, S. A. Klein, H.-y. Ma, S. Tang, K. Van Weverberg, C. J. Morcrette, and J. Petch, 2018: CAUSES: Diagnosis of the summertime warm bias in CMIP5 climate models at the ARM Southern Great Plains site. *J. Geophys. Res. Atmos.*, 123, 2968–2992, https://doi.org/10.1002/2017JD027200.
- Zhang, M. H., and Coauthors, 2005: Comparing clouds and their seasonal variations in 10 atmospheric general circulation models with satellite measurements. *J. Geophys. Res.*, **110**, D15S02, https://doi.org/10.1029/2004JD005021.
- Zhu, J., and X.-Z. Liang, 2013: Impacts of the Bermuda high on regional climate and ozone over the United States. *J. Climate*, **26**, 1018–1032, https://doi.org/10.1175/JCLI-D-12-00168.1.

Copyright of Journal of Climate is the property of American Meteorological Society and its content may not be copied or emailed to multiple sites or posted to a listserv without the copyright holder's express written permission. However, users may print, download, or email articles for individual use.